



Horizon 2020
Programme

METIS

Research and Innovation Action (RIA)

This project has received funding from the European
Union's Horizon 2020 research and innovation programme
under grant agreement No 945121

Start date : 2020-09-01 Duration : 57 Months

Influence of aftershocks and clustered seismicity on seismic fragility

Authors : Mrs. Paolo BAZZURRO (IUSS), Pablo García de Quevedo (IUSS), Nevena Sipcic (IUSS), Paolo Bazzurro (IUSS),
Shadi Fathabadi (TUK), Hamid Sadegh-Azar (TUK)

METIS - Contract Number: 945121

Project officer: Katerina PTACKOVA

Document title	Influence of aftershocks and clustered seismicity on seismic fragility
Author(s)	Mrs. Paolo BAZZURRO, Pablo García de Quevedo (IUSS), Nevena Sipcic (IUSS), Paolo Bazzurro (IUSS), Shadi Fathabadi (TUK), Hamid Sadegh-Azar (TUK)
Number of pages	40
Document type	Deliverable
Work Package	WP6
Document number	D6.7
Issued by	IUSS
Date of completion	2025-03-27 16:36:29
Dissemination level	Public

Summary

This report contains the methodologies and results for developing damage-state-dependent fragility curves, used for clustered seismicity. This report begins with a brief overview of the methodology employed for hazard-consistent mainshock-aftershock (MS-AS) record selection. Using the methods described in D5.2 we can obtain target spectra for the AS, given the MS hazard at site, which is then used to find matching AS records. The ground motions of MS and AS sequences are assembled in a back-to-back fashion to be utilized for nonlinear time history analysis of SSCs. Results of these analysis are classified, depending on the level of damage after the MS and used to fit fragility curves using the AS ground motion intensity. This methodology is applied to a simplified model of a Service Water Pump component, located within a reactor building. The results show a reduction of capacity of the component when compared to the MS-only case, which is dependent on the definition of the intermediate and collapse thresholds. Finally, this report also includes a set of practical recommendations for fragility assessment, based on tests related to the number of records employed, as well as a Bayesian updating methodology to reduce and optimize the number of stripes used.

Approval

Date	By
2025-04-14 13:40:50	Mrs. Mohamed ZOUATINE (TUK)
2025-04-14 14:30:29	Dr. Irmela ZENTNER (EDF)



METIS

Seismic Risk Assessment
for Nuclear Safety

Research & Innovation Action

NFRP-2019-2020

Influence of aftershocks and clustered seismicity on seismic fragility

Deliverable D6.7

Version N°2

Authors:

Pablo García de Quevedo, Nevena Šipčić, Paolo Bazzurro (IUSS)

Shadi Fathabadi, Hamid Sadegh-Azar (TUK)



Disclaimer

The content of this deliverable reflects only the author's view. The European Commission is not responsible for any use that may be made of the information it contains.



Document Information

Grant agreement	945121
Project title	Methods And Tools Innovations For Seismic Risk Assessment
Project acronym	METIS
Project coordinator	Dr. Irmela Zentner, EDF
Project duration	1 st September 2020 – 31 st May 2025 (57 months)
Related work package	WP 5- WP 6
Related task(s)	Task 6.7: Influence of aftershocks and clustered seismicity on seismic fragility
Lead organisation	IUSS
Contributing partner(s)	TUK, NTUA
Due date	29-10-2024
Submission date	X
Dissemination level	X

History

Version	Submitted by	Reviewed by	Date	Comments
N°1	Shadi Fathabadi	Saran Srikanth Bodda	22.11.2024	Sent revisions
N°2	Shadi Fathabadi	Saran Srikanth Bodda	14.03.2025	Comments addressed



Table of Contents

1.	Hazard-consistent MS-AS Record selection.....	9
1.1.	Selection for METIS case study.....	10
1.2.	Assembling of the sequences	11
2.	Damage-state-dependent fragility curves.....	12
2.1.	Application to SSC: Water pump	12
2.2.	Application to METIS case study: Diesel generator building in ZNPP.....	16
2.3.	Sensitivity analysis.....	25
2.3.1.	Case study: Water pump	25
3.	Practical recommendations for MS-only fragility assessment	26
3.1.	Determining the number of ground motions per stripe	26
3.1.1.	Selection of the ground motions	26
3.1.2.	Computation of the fragility curves.....	28
3.2.	Determination of the number of stripes for MSA	33
3.2.1.	Case study SSC: Service water pump	35
4.	Conclusions and Recommendations	36
5.	Acknowledgements	37
6.	Bibliography.....	37

List of figures

Figure 1 – Mainshock and Aftershock consistent conditional mean spectrum.	10
Figure 2 – Location of the METIS case study site	10
Figure 3 – Intensities of MS AS sequences and example of a back-to-back MS-AS ground motion pair	12
Figure 4 – Water pump model representation (a) EPRI water pump (taken from EPRI, 2018) (b) numerical model of the water pump and (c) 1D pushover response.....	13
Figure 5 – Mainshock response for MSA. MS-only fragility curve for DS1 and collapse for the intact structure.....	14
Figure 6 – Cloud of AS responses and linear regression fit depending on initial damage state. DS0 refers to the intact structure. Horizontal lines represent DS1 and collapse thresholds.	14



D6.7 Influence of aftershocks and clustered seismicity on seismic fragility

Figure 7 –Collapse fragility curve for the structure in the intact state (DS0) and in the intermediate damage state (DS1).....	15
Figure 8 –Diesel Generator Building 3D numerical model: a) Complex, b) Simplified MDOF.....	16
Figure 9 –Pushover Curves Comparison DGB Complex and Simplified model (Fixed-Base).....	17
Figure 10 –DGB Simplified model with soil springs and dashpots	17
Figure 11 – Pushover Curve for Top Floor Displacement of the DGB Simplified Model with SSI Consideration in <i>X</i> direction	18
Figure 12 – IM-EDP response of the DGB simplified model with SSI consideration for a set of 50 mainshock (MS) ground motions with PGA = 1g (from section 1), along with their corresponding mainshock-aftershock (MS-AS) sequences where aftershocks have a higher PGA.....	18
Figure 13 – Left: Hysteretic behavior of the simplified DGB model under a mainshock followed by a higher PGA aftershock; Right: mainshock-aftershock ground motion. 19	
Figure 14 – Comparison of DGB fragility curves: p_{MS} , $p_{AS MS}$ for DS0 (EDP: Top floor response acceleration, IM: PGA).....	19
Figure 15 – Comparison of the mean values for the target and sample distributions (50 records), using the conditional spectrum [Sa(0.01s)] derived for the METIS case study site, at an intensity level corresponding to a 0.001% probability of exceedance (POE) in 50 years.	20
Figure 16– Mainshock: a) IM-EDP; b) DGB Fragility curves for DS1, DS2 developed using MSA.....	21
Figure 17 – Left: Hysteretic behavior of the simplified DGB model under a strong mainshock followed by a higher PGA aftershock; Right: mainshock-aftershock ground motion.....	22
Figure 18 – a) Cloud of MS-AS responses with linear regression fit for DS1, b) Aftershock fragility curve for DS1 ($p_{AS}(EDP > DS1 MS)$).	23
Figure 19 – Comparison of DGB fragility curves: p_{MS} , p_{AS} and $p_{AS MS}$ for DS1. 23	
Figure 20 – a) Cloud of MS-AS responses with linear regression fit for DS2, b) Aftershock fragility curve for DS2 ($p_{AS}(EDP > DS2 MS)$).	24
Figure 21 – Comparison of DGB fragility curves: p_{MS} , p_{AS} and $p_{AS MS}$ for DS2. 24	
Figure 22 – Hazard curve for METIS case study.....	25
Figure 23 – Sensitivity analysis fragility curves resulting of changing the collapse threshold	26
Figure 24 – SSEs obtained for the three different IMLs using $S_a(1s)$ as an IM.....	27
Figure 25 – SSEs obtained for the three different IMLs using $S_a(0.1s)$ as an IM	28



Figure 26 – SSEs obtained for the three different IMLs using AvgS_a as an IM 28

Figure 27 – Monotonic backbone of the ModIMKP material model with damage states indicated..... 28

Figure 28 – Fragility curves obtained with 20 ground motion sets for three damage states ($\mu = 2, 3$ and 6 , from left to right). The figure shows the results for SDOF with $T_1 = 0.1s$ and $Sa(0.1s)$ as conditioning IM. 29

Figure 29 – Estimates of the fragility function parameters. Scatter points refer to 20 different iterations while solid lines connect the median values. Note: This figure shows the results obtained for the dynamic analysis of an SDOF with ModIMKP material model and $T_1=0.1s$ 30

Figure 30 – Ductility hazard curves obtained for sets of ground motion records with different number of accelerograms (from 3 to 44). Each panel shows curves from 20 different ground motions sets. Note: This figure shows the results obtained for the dynamic analysis of a SDOF with ModIMKP material model. 32

Figure 31 – Comparison of mean response hazard curves using different record selection variants in terms of ductility ratio and: (a) $Sa(T=1s)$, (b) $Sa(T=0.1s)$ and (c) AvgS_a as a conditioning IM. Note: This figure shows the results obtained for the dynamic analysis of a SDOF with ModIMKP material mode..... 32

Figure 32 – COV of estimated exceedance rates at different ductility levels and for different record sets: (a) $Sa(1s)$, (b) $Sa(0.1s)$ and (c) AvgS_a. Note: This figure shows the results obtained for the dynamic analysis of a 0.1s SDOF with ModIMKP material model. 32

Figure 33 - Example of interpolation to obtain the expected response for new IML 35

Figure 34 - Fragility curves per iteration, showing normal fit (with considered data) and Bayesian procedure 36

List of tables

Table 1: Values of the AvgSA at the 10 intensity levels at the METIS site. 11

Table 2 –Frequency Comparison between the DGB Complex and Simplified MDOF Model (Fixed-Base) 17

Table 3 – Values of the PGA for the 5 intensity levels at the METIS site..... 20

Table 4 – Intensity levels and conditioning Ims 27

Table 5 – COV in the fragility curve parameter estimates. Note: This table shows the results obtained for the dynamic analysis of an SDOF with ModIMKP material and $T_1=0.1s$ 30

D6.7 Influence of aftershocks and clustered seismicity on seismic fragility





Abbreviations and Acronyms

Acronym	Description
WP	Work Package
MS	Mainshock
AS	Aftershock
CS	Conditional Spectrum
IM	Intensity Measure
SSC	Structures, Systems And Components
PGA	Peak Ground Acceleration
NPP	Nuclear Power Plant
SSI	Soil-Structure Interaction
DGB	Diesel Generator Building
MSA	Multiple Stripe Analysis
MLE	Maximum Likelihood Estimation
ETAS	Epidemic-Type Aftershock Sequence
GMPE	Ground Motion Prediction Equation
IMLs	Intensity Measure Levels
ZNPP	Zaporizhzhia Nuclear Power Plant

Summary

This report contains the methodologies and results for developing damage-state-dependent fragility curves, used for clustered seismicity. This report begins with a brief overview of the methodology employed for hazard-consistent mainshock-aftershock (MS-AS) record selection. Using the methods described in D5.2 we can obtain target spectra for the AS, given the MS hazard at site, which is then used to find matching AS records. The ground motions of MS and AS sequences are assembled in a back-to-back fashion to be utilized for nonlinear time history analysis of SSCs. Results of these analysis are classified, depending on the level of damage after the MS and used to fit fragility curves using the AS ground motion intensity. This methodology is applied to a simplified model of a Service Water Pump component, located within a reactor building. The results show a reduction of capacity of the component when compared to the MS-only case, which is dependent on the definition of the intermediate and collapse thresholds. Finally, this report also includes a set of practical recommendations for fragility assessment, based on tests related to the number of records employed, as well as a Bayesian updating methodology to reduce and optimize the number of stripes used.

Keywords

Fragility, Clustered Seismicity, Aftershocks, Damage states



Introduction

Recently, several seismic sequences (e.g., Christchurch 2011, Central Italy 2016-2017, Turkey 2023) showed that the earthquake sequences pose an additional risk to society as the financial losses increase when compared to cases characterized by only one main event (i.e., mainshock only cases). While not as common, several power plants have also been impacted in the past by some sequences (e.g., Chile 1985, Alaska 1986, Turkey 1999, Tohoku 2011), where there have been observations of increased damage to structures or subsystems that were already damaged on the mainshock event. Even though these cases are few and data of additional damage to nuclear power plants due to sequences are scarce, the effect and increase in risk they pose should not be underestimated a priori.

Traditional approaches for seismic risk assessment focus solely on mainshocks, a practice that may lead to underestimation of seismic risk. This is the case especially in the aftermath of major events that, invariably, are followed by a cluster of aftershocks, several of which could be of large magnitude and cause further damage. This issue has been long recognized and several researchers have been studying how to incorporate clustered seismicity into risk assessment both in terms of hazard and vulnerability.

This report will present the procedure to assess the changes in fragility due to MS sustained damage on SSCs, through the development of damage-state-dependent fragility curves. These curves are made hazard-consistent through careful MS AS record selection, which produces realistic MS AS sequences that adhere to the properties observed in real cases.

1. Hazard-consistent MS-AS Record selection

Record selection of hazard-consistent MS AS sequences is required due to the scarcity of recording of real MS-AS sequences at several levels of ground motion intensity. This selection makes it possible to conduct nonlinear time history analysis that would help evaluate both the responses of the structures at the end of a sequence, as well the responses to AS of different ground motion intensity of structures with different levels of MS-caused damage.

The procedure for MS-AS consistent record selection comes from Papadopolous et al 2020, and is detailed in depth in Deliverable 5.2. Therefore, only a brief summary will be included here.

The process begins by selecting MS records using the Conditional Spectrum (CS) approach, as explained in Section 1.2 of D5.1. Records are selected to match the target distribution in terms of spectral ordinates conditioned on the value of the chosen intensity measure IM^* at the hazard level of interest. Seismic hazard disaggregation is then performed to identify the scenarios (in terms of magnitude M , distance R and residual ϵ for the chosen IM^* level) that contribute to the exceedance of that IM^* level. Each record is assigned a random rupture scenario based on the disaggregation probability mass function for the IM^* level. A random realization of a MS ground motion response spectrum is created by selecting correlated $\ln(Sa)$ values from a multivariate normal distribution. Then, a record is chosen from the database that closely matches this realization. The simulation procedure is repeated several times to assemble the set of MS records that best matches the target distribution. The requirement of rupture information is crucial to generate the sequences and this is the main reason why we do not use the procedure proposed by (Jayaram et al., 2011) described in Section 1.1 of D5.1.

The next step involves generating realistic aftershock sequences using the M and R values of each selected MS ground motion. One approach, as suggested by Papadopoulos et al. 2020, involves using the Epidemic-Type Aftershock Sequence (ETAS) model proposed by Ogata (1988) to generate sequences assuming that the MS is the parent event.

To select the AS ground motions, it is necessary to find the distribution of the AS spectral accelerations at different periods of vibration conditional on the spectral accelerations of the specific MS record and the values of Magnitude and rupture-to-site distance of the MS. We use the MSAS-CS technique, developed by Papadopoulos et al. (2020) to derive the joint distributions of spectral accelerations at multiple periods, which is well represented by a multivariate lognormal distribution. This technique needs the adoption of a Ground Motion Prediction Equation (GMPE), which in this report is Kotha et al.,

2020 and Lanzano et al., 2019, as determined adequate for the site and used in the PSHA analysis. Finally, using this correlation between MS and AS, we can derive a MS-consistent AS ground motion conditional spectrum, such as the one shown in Figure 1.

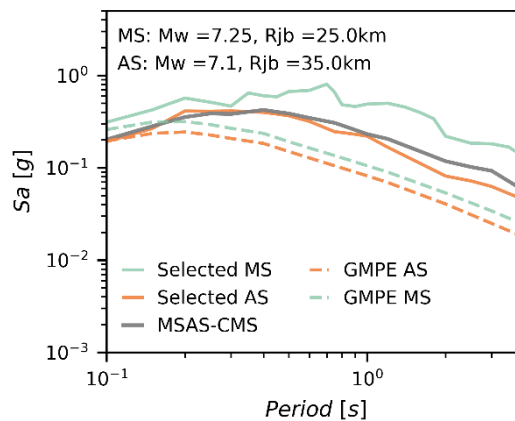


Figure 1 – Mainshock and Aftershock consistent conditional mean spectrum.

Having the MS-consistent AS target, a realization of the AS response spectrum is sampled from the joint AS Sa distribution followed by the selection of the ground motion (scaled, if needed) that best matches the target spectrum. For computational simplicity, only one realization of the AS ground motion is drawn in this exercise. As many selected AS ground motions will have very low intensity, one can set a threshold below which all sampled GMs are discarded, and the simulation is repeated. As shown by (Papadopoulos et al. 2020) the potential bias is not expected to be of importance as long as the intensity threshold for discarding is kept reasonably low, i.e., the small magnitude and/or large distance MS ruptures are not forced to produce AS sequences with unrealistically large M and associated ground motions. For more details regarding the MSAS-CS procedure briefly discussed here, see D5.2 and Papadopoulos et al. 2020.

1.1. Selection for METIS case study

MS and AS consistent record selection was performed for the METIS case study site shown in Figure 2. The original MS selection consisted of 10 ground motion intensity measure levels (IMLs), representing return periods going from 40 to 100 000 years. Table 1 shows the different IMLs considered in the case study, along with their corresponding intensity value, in terms of average spectral acceleration ($AvgSa$). The choice of this intensity measure was based on the nature of this type of analyses, where we expect the structures to sustain some damage, and therefore, the spectral acceleration at the fundamental period of the elastic structure would no longer be an accurate predictor of the response given the demand.

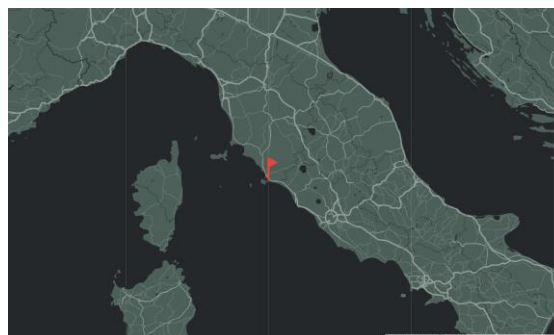


Figure 2 – Location of the METIS case study site

Here, for each IML we selected 50 MS ground motions to match the target CS spectrum, following the methodology described previously. The higher number of MS records, compared to the MS-only selection

is required to generate enough sequences to obtain high intensity AS motions, as a limited set would result in too few motions capable of damaging structures.

IML	poe in 50 years	<i>AvgSa</i> (0.1:0.4s) [g]
1	0.7180	0.019
2	0.2855	0.049
3	0.0998	0.097
4	0.0488	0.147
5	0.0198	0.242
6	0.0100	0.347
7	0.0050	0.491
8	0.0025	0.683
9	0.0010	1.023
10	0.0005	1.364

Table 1: Values of the AvgSA at the 10 intensity levels at the METIS site.

For each record associated with a MS earthquake ground motion, the sequence of AS events is simulated using the ETAS model, using parameters calibrated for Central Italy (Šipčić et al., 2022). For every AS in the sequence, we defined the target spectrum of the ground motion at the site using the Papadopoulos et al. 2020 methodology. We consider only AS events that are triggered in the period of one year after the MS, with a minimum magnitude of 3.5 and within a radius of 100km. Only ground motions with *AvgSa* higher than 0.2g are retained.

1.2. Assembling of the sequences

The MS and AS consistent record selection resulted in a large set of seismic sequences with a maximum of 20 AS ground motions allowed for each of the 50 MS records to limit the number of analyses. The intensities of each MS AS pair used herein are shown in Figure 3. The figure only shows the results for the last 5 levels of intensity (IMLs 6 to 10), as these are the levels that could cause structural damage (post-yield) to the considered structure and are the ones kept for analysis. Here, we can observe how the selection results in stripes at the five MS intensity, each one with a distribution of AS intensities. The total number of sequences, consisting of the five IMLs considered, with 50 MS records per IML and a variable number of AS per MS resulted in 1341 pairs. The median causative parameters resulting of the record selection of the set used herein can be found in **Table 2**. Each MS and AS pair of records was assembled back-to-back, as shown in Figure 3, leaving 10 seconds between signals to allow the structure to come to rest and damp any remaining cycles from the MS motion. For compatibility, in some cases one of the signals had to be resampled to have the same *dt* of the other corresponding record. In this resampling exercise we kept the largest *dt* of the two. These sequences are only used to derive fragility curves and not to perform real time simulations of damage.

1 IML	2 poe in 50 years	3 <i>AvgSa</i> (0.1:0.4s) [g]	4 <i>Mw</i>	5 <i>Rjb</i> [km]
6	7	8	9	10
11	12	13	14	15
16	17	18	19	20



21	22	23	24	25
26	27	28	29	30
31 6	32 0.0100	33 0.347	34 5.47	35 15
36 7	37 0.0050	38 0.491	39 5.45	40 12
41 8	42 0.0025	43 0.683	44 5.62	45 10
46 9	47 0.0010	48 1.023	49 5.50	50 8.5
51 10	52 0.0005	53 1.364	54 5.55	55 8.0

56 Table 2: Values of the AvgSA at the considered intensity levels at the METIS site and median causative parameters found from disaggregation.

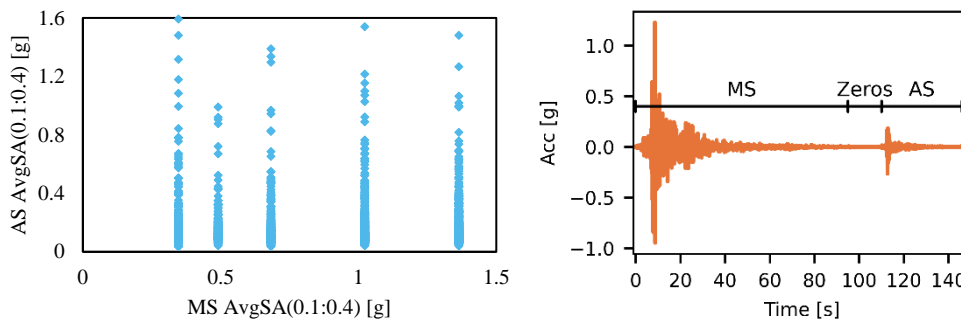


Figure 3 – Intensities of MS AS sequences and example of a back-to-back MS-AS ground motion pair

2. Damage-state-dependent fragility curves

2.1. Application to SSC: Water pump

This section will focus on the methodology used to derive the damage-state-dependent fragility curves. The curves can be derived for different SSCs as long as there is information available regarding intermediate damage states. Here we will focus on a service water pump, represented in Figure 4a, placed inside an AP 1000 advanced reactor. This reactor includes a Coupled Auxiliary and Shield Building (ASB), a Steel Containment Vessel (SCV), and a Containment Internal Structure (CIS). The water pump is modeled as a 3-dimensional stick with a single mass (Figure 4b), located at the top of the reactor, featuring a fundamental period (T_1) of 0.10 seconds, a yield displacement of 2.3 mm, and originally assumed failure at a ductility (μ) of 1.25 (Figure 4c). Its nonlinear behavior is represented by an elastic-perfectly-plastic force-deformation backbone with some pinching behavior. All components are modeled in OpenSees, utilizing data from EPRI (2018).

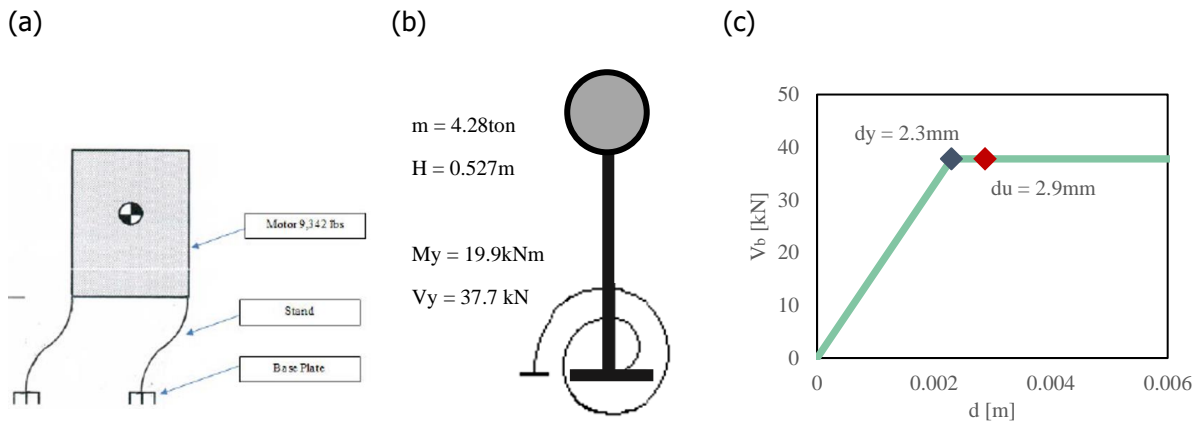


Figure 4 – Water pump model representation (a) EPRI water pump (taken from EPRI, 2018) (b) numerical model of the water pump and (c) 1D pushover response

The MS-AS sequences assembled in the previous section are then successively applied to the water pump structure for response assessment via nonlinear time-history analyses. Here we capture the damage states (DSs) that the structure experiences after the MS and after the entire sequence. In this illustrative example, we consider the structure to experience only three possible damage states after an earthquake: DS0 (undamaged conditions), DS1 (intermediate damage state that may correspond to malfunctioning of the water pump), and DS2=C=collapse (ultimate damage state corresponding to complete loss of functionality). The onset of DS1 and DS2=C is defined by the maximum displacement of the component. Due to the lack of any specific information, we assume that the water pump is in DS1 after yield (displacement $\geq 2.3\text{mm}$), while for the collapse threshold, we increased the maximum ductility to 2.5 to sufficiently differentiate DS1 from DS2= Collapse. The influence of this increase and the DS1 threshold can be found in the next subsection. Given that in this example there is only one intermediate DS, i.e. DS1, we can only compute one DS-dependent fragility curve namely the fragility curve for collapse caused by the aftershock given DS1 after the mainshock. Of course, we can also develop two fragility curves for the undamaged conditions, one for DS1 and one for DS2=Collapse. It must be noted that the use of peak inelastic displacement may be suboptimal to detecting the accumulation of damage in some cases (Baraschino et al 2023), such as those of structures which may be subjected to significant degradation. This would lead to the necessity of using more complex damage measures that have a monotonically increasing behavior (such as the Park and Ang Damage Index, 1985) which would require calibration through numerical experiments. However, most nuclear structures and components are made of better performing materials which make them less susceptible to this degradation.

In the case of MS, the responses of the structure plotted against the ground motion IM ($AvgSA$) form "stripes" at the selected mainshock IM levels, as shown in Figure 5a. In the case of AS, however, the response data points scatter like a "cloud" because they represent random responses conditioned on the mainshock event, as shown in Figure 6. Here the responses measured by the engineering demand parameter (EDP) corresponding to the maximum displacement recorded at the top of the water pump structure.

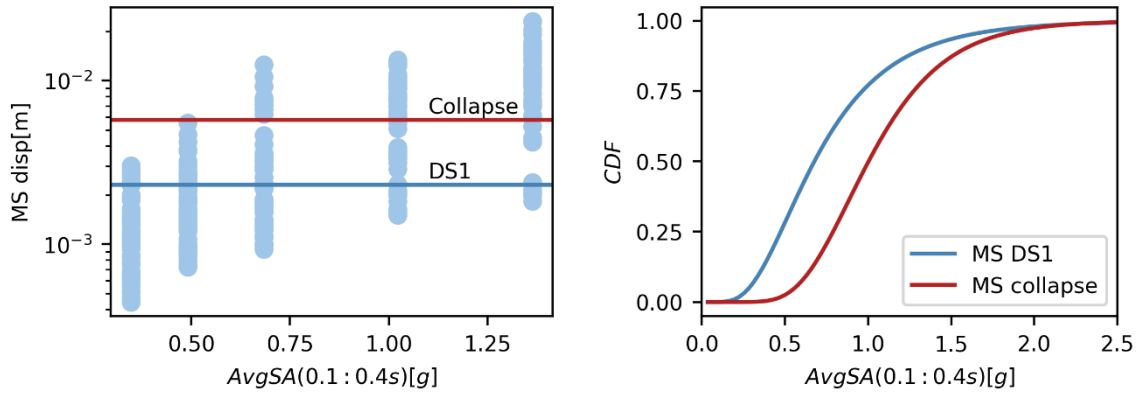


Figure 5 – Mainshock response for MSA. MS-only fragility curve for DS1 and collapse for the intact structure

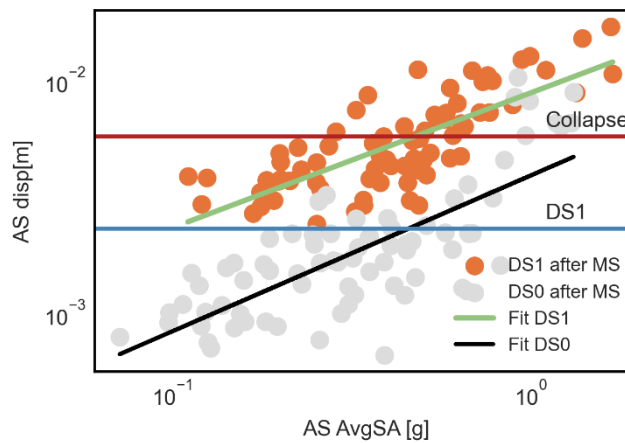


Figure 6 – Cloud of AS responses and linear regression fit depending on initial damage state. DS0 refers to the intact structure. Horizontal lines represent DS1 and collapse thresholds.

To develop the two fragility functions for the undamaged building we used the lognormal cumulative distribution functions derived statistically from the analysis of the mainshock responses. The parameters of these MS fragilities for every DS are found through a *MLE* (Baker, 2015), following the Multiple Stripe Analysis (*MSA*, Jalayer and Cornell, 2009) methodology using only the unique MS responses (i.e., 50 per stripe). Figure 5a illustrates how the fragility curves are obtained for MS only seismicity through this approach. There we can see when the onset of both damage states is exceeded as well as the resulting fragility curves (Figure 5b). The median collapse capacity is 1.0g and 0.35 is its log standard deviation. regarding DS1 the acceleration median capacity is 0.67g with a log standard deviation of 0.52.

To develop the damage-state-dependent fragility function for aftershocks, i.e., $C|DS1$, we first categorize the damage states of the structure following each mainshock according to the values of the EDP chosen (here maximum displacement). This first step separates the mainshock runs into three different subsets: Those that left the structure undamaged (DS0), those that brought it to the intermediate damage state (DS1) and those that collapse it. Then we identify all mainshock events that brought the structure to DS1 and then monitor its response after the AS. This analysis provides a set of AS intensity-response pairs (or *IM-EDP*) given DS1 after the MS, which are used to derive damage-dependent fragility functions. To do so there are various statistical methods, such as linear regression or MLE. Figure 6 shows the AS *IM-EDP* relation (in this case taken as maximum displacement) of a structure, classified as DS0 if it did not exceed the DS1 threshold during the MS, and DS1 if it did. In this case, we perform linear regression on log space for the *IM-EDP* space, as shown in Equation (1), following the methodology of cloud analysis proposed by Jalayer (2003). Here $\eta_{1/Sa}$ is the median



response (Y) given the intensity (IM), while a and b are the constants found through linear regression. Results of this linear regression can then be used to obtain the mean capacity, found at the point of interception between the fitted line and the defined collapse threshold (horizontal red line in Figure 6), and the curves logarithmic standard deviation ($\sigma_{\log Y|IM}$) is found through the fit error between $\eta_{Y|S_a}$ all n data points, as shown in Equation (2).

$$E[\log Y|IM] = \log \eta_{Y|IM} = \log a + b \log IM \tag{1}$$

$$\sigma_{\log Y|IM} = \sqrt{\frac{\sum_{i=1}^n (\log Y_i - \log \eta_{Y|IM})^2}{n - 2}} \tag{2}$$

Figure 7 shows the damage-state-dependent fragility curve obtained from this analysis. Here, we employ the cloud method in the cases where the component is in DS1 after the MS and we observe an increase in displacement during the AS. Here, the median collapse capacity becomes 0.47g with a log dispersion of 0.30. This large decrease in median capacity happens since the limit states (intermediate damage, DS1, and DS2=collapse) are very close together, ductility-wise. Hence, while in DS1 even aftershocks with small intensity are sufficient to push the structure into the collapse state, as defined here. This conclusion, however, should not be generalized without hard data of what constitutes an intermediate damage state of this water pump and of other components. The current literature shows a lack of data regarding intermediate damage states for different components, because it a customary practice to consider only two states: DS0 (namely intact structure and, therefore, operational) and failure (namely C, which in this case simply means non-operational).

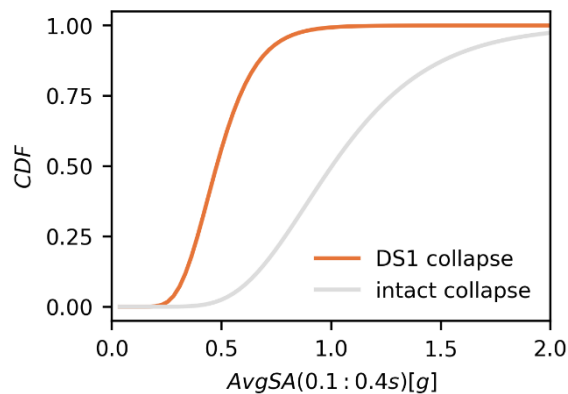


Figure 7 –Collapse fragility curve for the structure in the intact state (DS0) and in the intermediate damage state (DS1) for clustered seismicity analysis

2.2. Application to METIS case study: Diesel generator building in ZNPP

The Diesel Generator Building (DGB) is one of the most critical structures within the SSCs of a nuclear power plant. Its failure or malfunction could have a direct impact on plant safety, especially during or after a seismic event, or throughout the safe shutdown process. The DGB of ZNPP is represented by a complex 3D numerical model, which, to reduce the computational cost of the main shock-aftershock (MS-AS) analysis, has been simplified into a 3D multi-degree-of-freedom (MDOF) stick model (Figure 8). To accurately capture its nonlinear behavior, pushover analysis was conducted in both the X and Y directions. Incremental forces were applied at the top of the building, generating force-displacement curves for each direction. These curves were simplified into equivalent bilinear form according to FEMA guidelines (ASCE, 2000), and converted into moment-curvature relationships, which were incorporated into the model as two springs at the base of the DGB's MDOF system. The system's properties, such as stiffness and cross-sectional area, were calculated to ensure the simplified model's modal characteristics were consistent with those of the original complex model. Figure 9 compares the pushover curves of the complex and simplified models. Table 3 shows the frequency of the DGB complex and simplified model in 3 main modes.

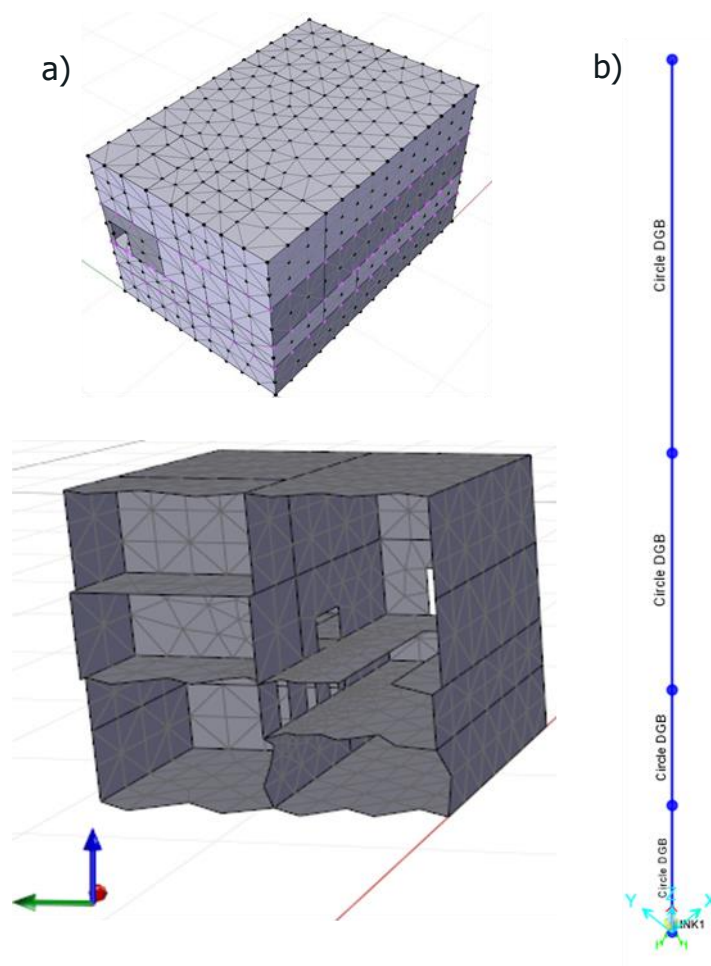


Figure 8 –Diesel Generator Building 3D numerical model: a) Complex, b) Simplified MDOF

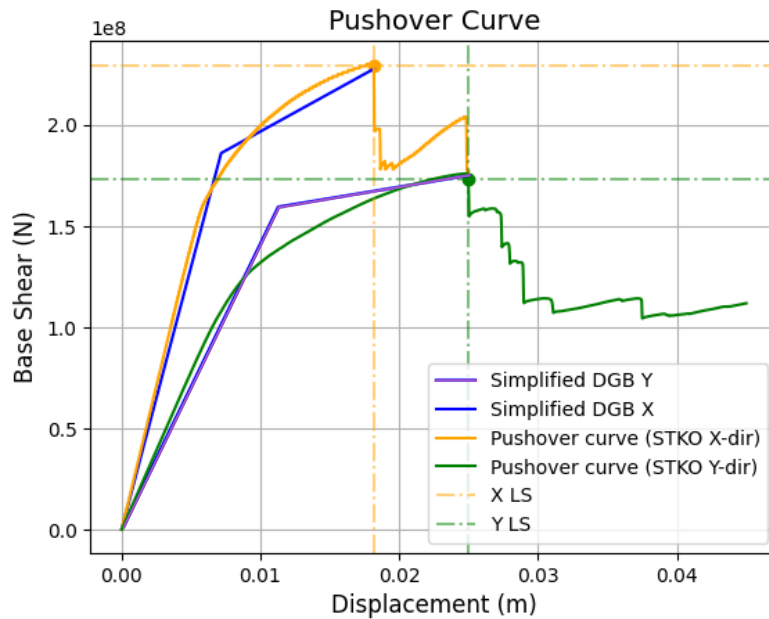


Figure 9 –Pushover Curves Comparison DGB Complex and Simplified model (Fixed-Base)

Table 3 –Frequency Comparison between the DGB Complex and Simplified MDOF Model (Fixed-Base)

Mode	MDOF Frequency (Hz)	Complex Frequency (Hz)
1 Y	12.0061	12.00
2 X	16.2727	16.27
3 Z	32.71	32.72

The Soil-Structure Interaction (SSI) is also considered in the simplified model by incorporating equivalent springs and dampers in all three directions (Figure 10) using substructure approach (FEMA 440, 2005), based on the soil profile of the METIS case study site (for detailed information on the soil column, refer to the D5.4 report).

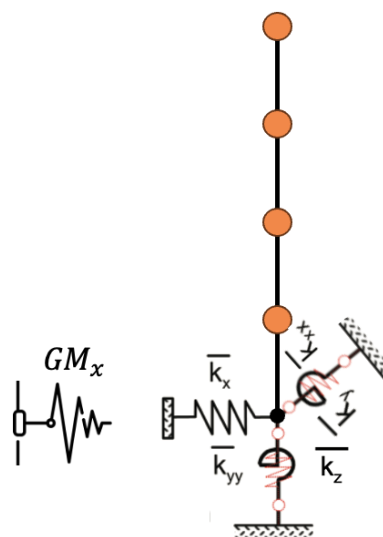


Figure 10 –DGB Simplified model with soil springs and dashpots



Nonlinear time history analysis was performed in OpenSees (McKenna, 2000), utilizing Hysteretic material to model the nonlinear behavior of the springs, which were defined to replicate the behavior of the complex model. Three damage states are considered for the DGB after the mainshock: DS0 = 0.006 m represents the undamaged structure, DS1 = 0.020 m indicates an intermediate level of damage, and DS2 = 0.034 m represents the collapsed structure (Figure 11).

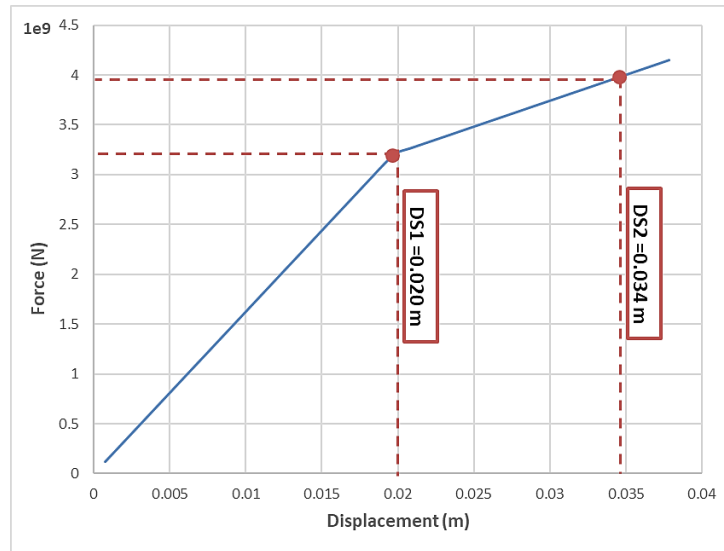


Figure 11 – Pushover Curve for Top Floor Displacement of the DGB Simplified Model with SSI Consideration in X direction

If the same set of ground motions (GMs) from Section 1 is used, the displacement caused by the mainshock remains minimal and does not push the structure beyond the linear behavior range, as shown in Figure 12. Figure 13 illustrates the hysteretic response of the simplified DGB model when subjected to a mainshock followed by an aftershock with a higher peak ground acceleration (PGA). The results indicate that the structure remains within the linear range during the mainshock and, even with the subsequent higher-PGA aftershock, no additional damage occurs beyond the initial mainshock impact. This suggests that after a weak mainshock, the structure returns to its undamaged state within the time span between the mainshock and aftershocks. Furthermore, even when the aftershock PGA exceeds that of the mainshock ($PGA_{AS} > PGA_{MS}$), the structure does not transition into the nonlinear range.

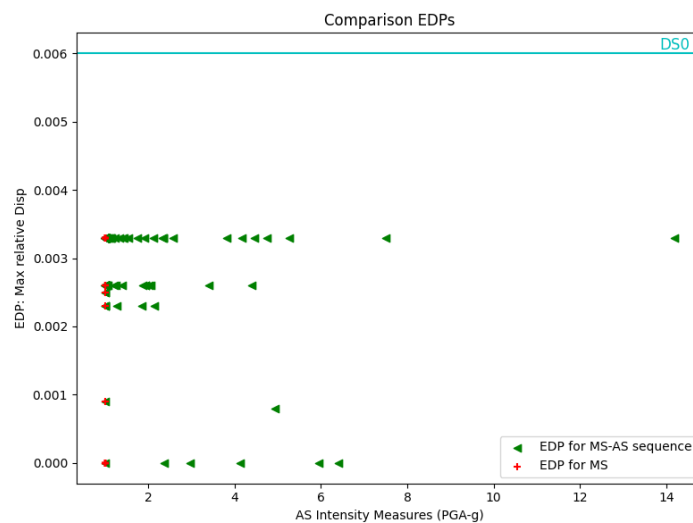


Figure 12 – IM-EDP response of the DGB simplified model with SSI consideration for a set of 50 mainshock (MS) ground motions with PGA = 1g (from section 1), along with their corresponding mainshock-aftershock (MS-AS) sequences where aftershocks have a higher PGA.

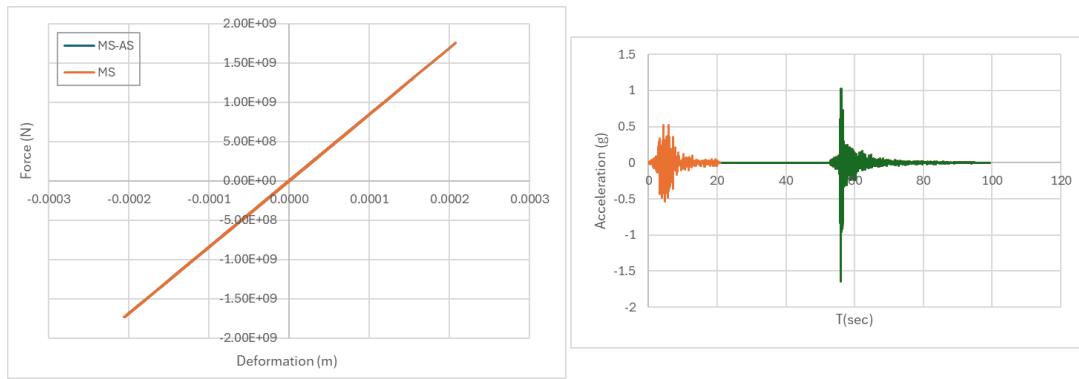


Figure 13 – Left: Hysteretic behavior of the simplified DGB model under a mainshock followed by a higher PGA aftershock; Right: mainshock-aftershock ground motion.

However, it is important to note that even when the structure remains within the linear range, the floor accelerations induced by the MS-AS sequence can exceed those from the mainshock alone, depending on the aftershock characteristics such as PGA and duration. Consequently, the floor response spectrum for MS-AS may exhibit higher values than for MS alone, which is particularly relevant for the performance of equipment and systems located at different floors within the DGB. As shown in Figure 14, when considering response acceleration at the top floor of the DGB as the engineering demand parameter (EDP) and PGA as the intensity measure (IM), the failure probability based on the METIS hazard curve and the same set of ground motions from Section 1, decreases from 1.583g to 1.281g. The corresponding acceleration associated with the displacement of the top floor is considered the limit state for DS0. This finding highlights that structural failure is not necessarily the primary concern; rather, the performance of equipment, components, and pipelines within the DGB must also be considered.

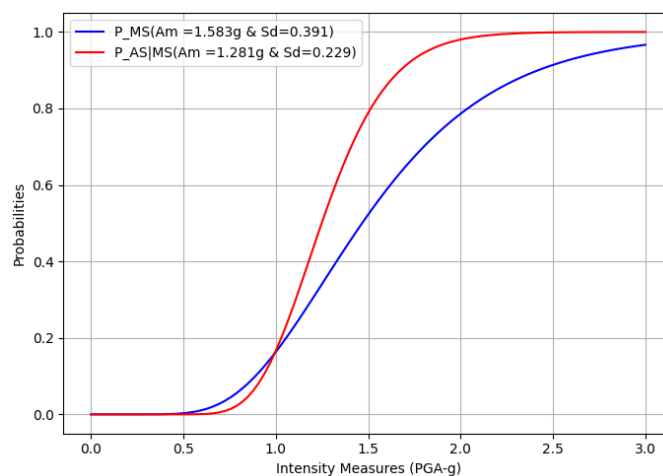


Figure 14 – Comparison of DGB fragility curves: p_{MS} , $p_{AS|MS}$ for DS0 (EDP: Top floor response acceleration, IM: PGA).

In practice, the DGB is designed for linear behavior, with failure criteria primarily linked to the functionality of non-structural components rather than structural damage to the building itself. This implies that the failure point of the DGB is more closely related to serviceability or safety functions rather than structural collapse, aligning it with Damage State 0 (DS0) rather than DS1 or DS2.

To assess the structural failure of the DGB, and given its robustness, a second set of ground motions with higher return periods, specific to the METIS case study site, was selected using the same methodology outlined in the previous section for mainshock–aftershock (MS-AS) sequences. This approach ensures that the building's response extends into the nonlinear range. The use of rare high-intensity ground motions in this study is primarily intended to demonstrate the methodology for incorporating aftershocks into seismic safety assessments of nuclear power plants (NPPs). Table 4



presents the various Intensity Measure Levels (IMLs) considered in this case study, along with their corresponding intensity values in terms of PGA. Figure 15 compares the mean values of the target and sample distributions, derived from a set of 50 records based on the conditional spectrum [Sa (0.01s)] for the METIS case study site. This comparison is evaluated at an intensity level corresponding to a 0.001% probability of exceedance over a 50-year period, providing a basis for the fragility assessment under rare seismic events.

Table 4 – Values of the PGA for the 5 intensity levels at the METIS site

IML	Poe in 50 years (%)	PGA (Sa (0.01s)) [g]
1	0.00350	1.96
2	0.00100	2.79
3	0.00020	4.01
4	0.00017	4.18
5	0.00015	4.37

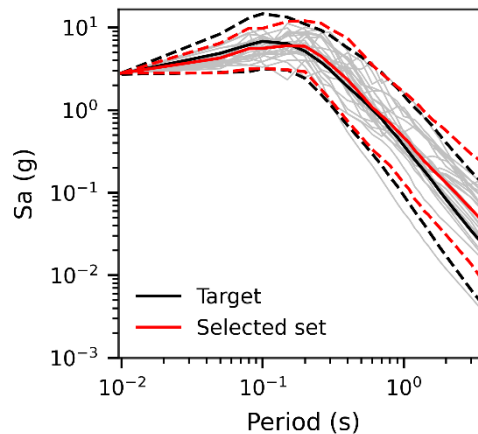


Figure 15 – Comparison of the mean values for the target and sample distributions (50 records), using the conditional spectrum [Sa (0.01s)] derived for the METIS case study site, at an intensity level corresponding to a 0.001% probability of exceedance (POE) in 50 years.

To develop damage-state-dependent fragility curves for the DGB under mainshock-aftershock (MS-AS) sequences, the linear regression method (Cornell et al, 2002), in conjunction with the multiple stripe analysis (MSA) method (Jalayer and Cornell, 2009), is employed to estimate the fragility parameters (median and standard deviation) for the mainshock, using 50 MS records per stripe. The maximum relative displacement of the top floor with respect to the bottom node is considered as the engineering demand parameter (EDP), while peak ground acceleration (PGA) is used as the intensity measure (IM) of the ground motions (Figure 16a).

The estimated median (A_m) of the mainshock fragility curve for DS1 is approximately 5.701g, with an estimated standard deviation (σ) of 0.212. Furthermore, the values for DS2 are 8.774g for the median and 0.212 for the standard deviation (Figure 16b).

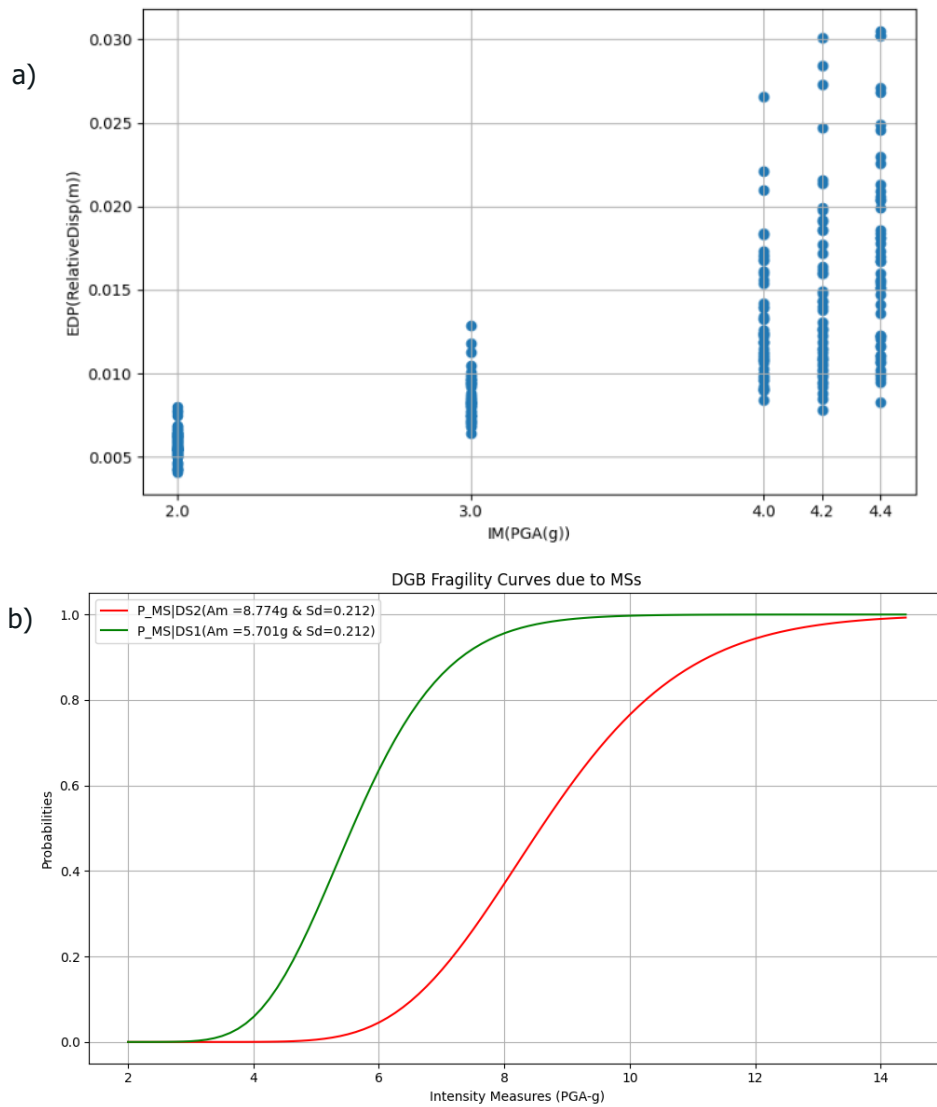


Figure 16– Mainshock: a) IM-EDP; b) DGB Fragility curves for DS1, DS2 developed using MSA.

To develop damage-state-dependent fragility curves for MS-AS sequences, the mainshock records are categorized into three groups based on the DGB structure's response following the mainshock. Group 1 includes records where $EDP < DS1$, Group 2 with $DS1 \leq EDP < DS2$, and Group 3 where $EDP \geq DS2$ (collapse). Since the DGB structure has already collapsed for the Group 3 mainshock records, these are excluded from the MS-AS analysis. We then used the set of MS-AS records corresponding to Group 1 mainshock records to develop the AS fragility curve for DS1 ($p_{AS|MS}(EDP > DS1|MS)$), and Group 2 mainshock records to develop AS fragility curve for DS2 ($p_{AS|MS}(EDP > DS2|MS)$). In this case, linear regression is performed in log space for the IM-EDP relationship, as shown in Equation (1) in Section 2.1, and in Figure 18a for Group 1 ground motions and Figure 20a for Group 2 ground motions, following the cloud analysis methodology proposed by Jalayer (2003). The median and standard deviation of the fragility curve for DS1 are estimated to be 4.472g and 0.234, respectively (Figure 18b). Figure 19, compares the fragility curves for $p_{MS} = p(EDP > DS1)$, $p_{AS|MS} = p(EDP > DS1|MS)$, $p_{MSAS|MS} = p_{MS} + (1 - p_{MS}) \times p_{AS|MS}$. Furthermore, the median and standard deviation of the fragility curve for DS2 are estimated to be 5.3g and 0.096, respectively (Figure 20b). Figure 21 presents a comparison of p_{MS} , $p_{AS|MS}$ and $p_{MSAS|MS}$.

Figure 17 illustrates the hysteretic response of the simplified DGB model under a strong mainshock followed by an aftershock with a higher PGA. As shown, the structure remains in the linear range after

the mainshock, but the stronger aftershock pushes the structure into its nonlinear range, resulting in additional damage in the MS-AS sequence.

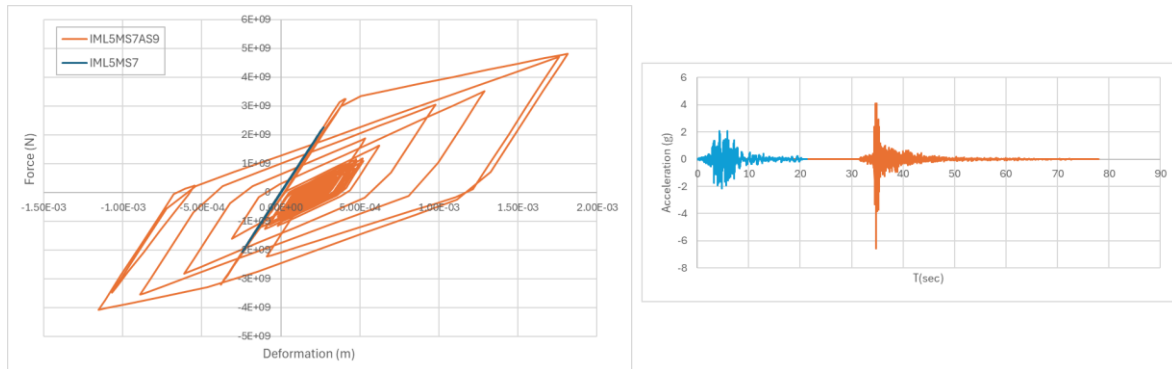


Figure 17 – Left: Hysteretic behavior of the simplified DGB model under a strong mainshock followed by a higher PGA aftershock; Right: mainshock-aftershock ground motion.

As previously discussed, DS1 and DS2 failure points are associated with extremely rare earthquake scenarios. Figure 22 illustrates the hazard curve for the METIS case study, showing that the annual exceedance rate for $PGA > 3$ is nearly zero ($< 10^{-7}$). For a given fragility curve, we can also calculate the annual collapse rate of the structure ($\lambda_{collapse}$) using the following method (Baker, 2015):

$$\lambda_{collapse} = \int_x P(C|IM = x) |d\lambda_{IM}(x)|$$

Where $\lambda_{IM}(x)$ represents a ground motion hazard curve, indicating the annual rate of exceedance for ground motions with $IM > x$, and $|d\lambda_{IM}(x)|$ is the absolute value of the derivative of the hazard curve. Based on the METIS hazard curve, the annual collapse rate of the DGB structure ($\lambda_{collapse}$) for DS1 is approximately 2.36×10^{-8} . This indicates that the annual probability of failure for the DGB structure under mainshock-aftershock (MS-AS) sequences remains very low. However, our analysis demonstrates that the effects of aftershocks on fragility of a DGB already damaged by mainshocks are not negligible. Given the rarity of these MS-AS scenarios, the resulting annual collapse rate is effectively minimal.

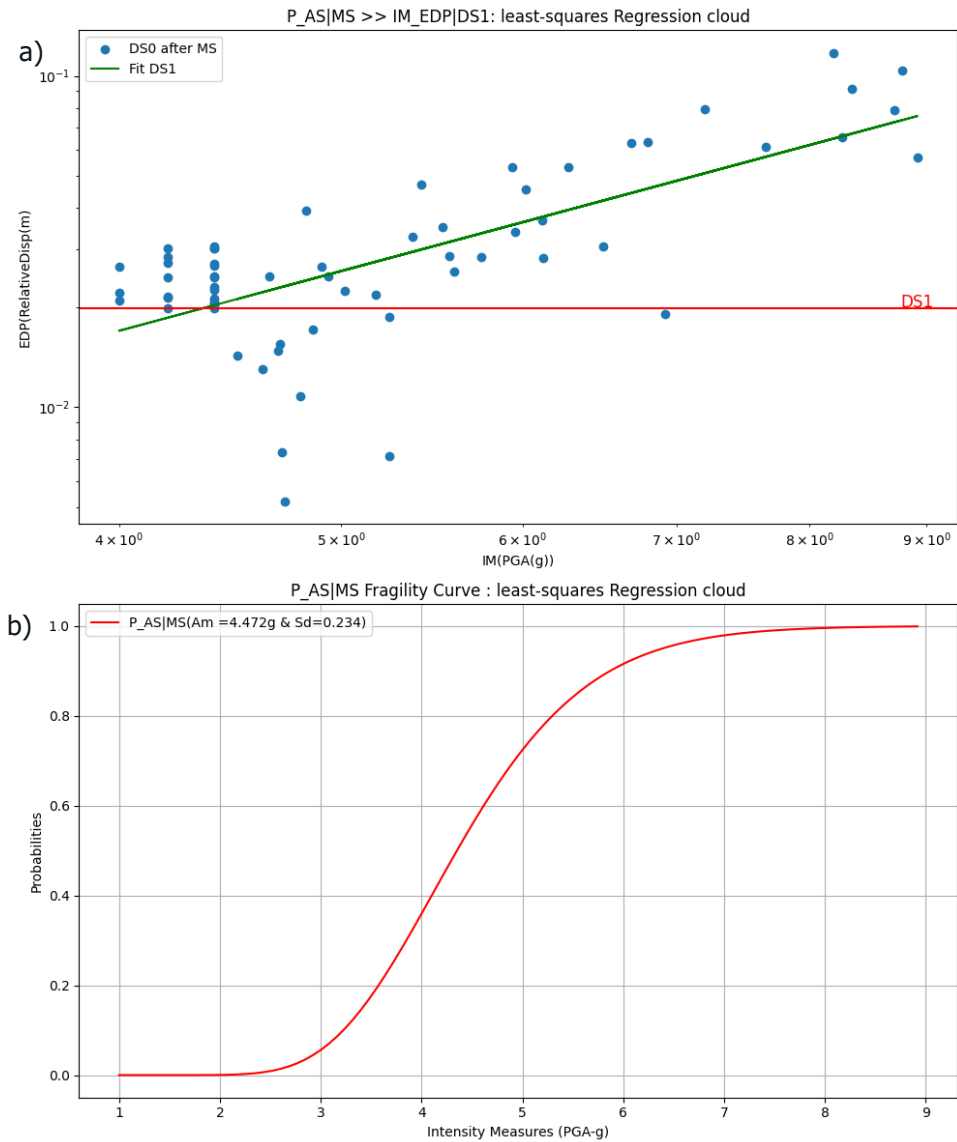


Figure 18 – a) Cloud of MS-AS responses with linear regression fit for DS1, b) Aftershock fragility curve for DS1 ($p_{AS|MS}(EDP > DS1|MS)$).

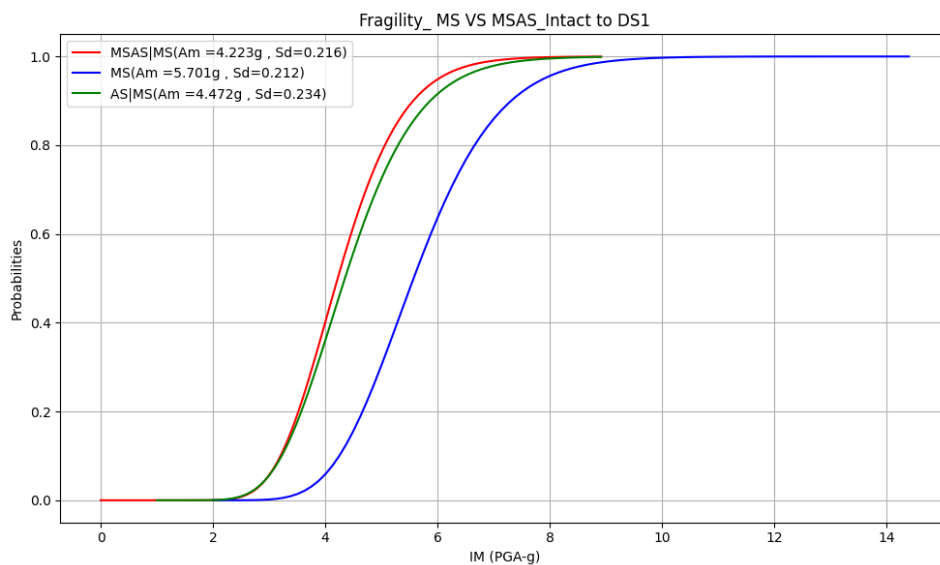


Figure 19 – Comparison of DGB fragility curves: p_{MS} , $p_{AS|MS}$ and $p_{MSAS|MS}$ for DS1.

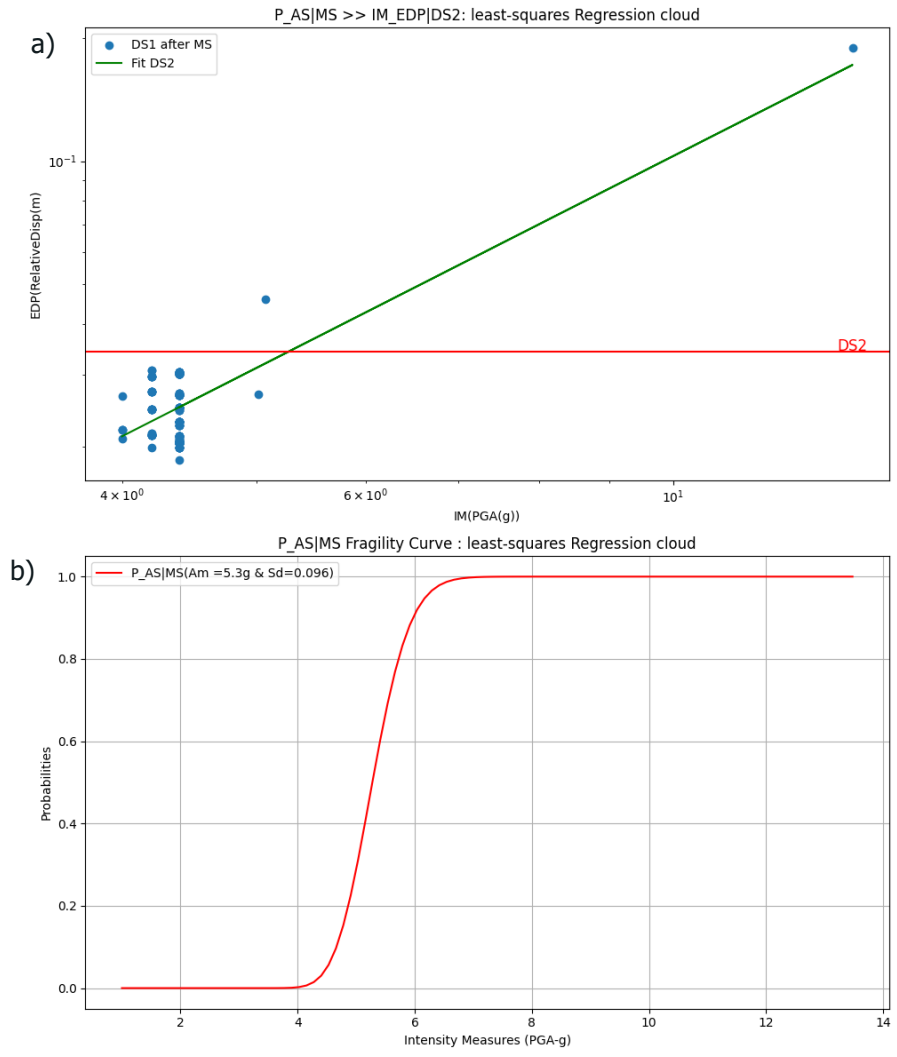


Figure 20 – a) Cloud of MS-AS responses with linear regression fit for DS2, b) Aftershock fragility curve for DS2 ($p_{AS|MS}(EDP > DS2|MS)$).

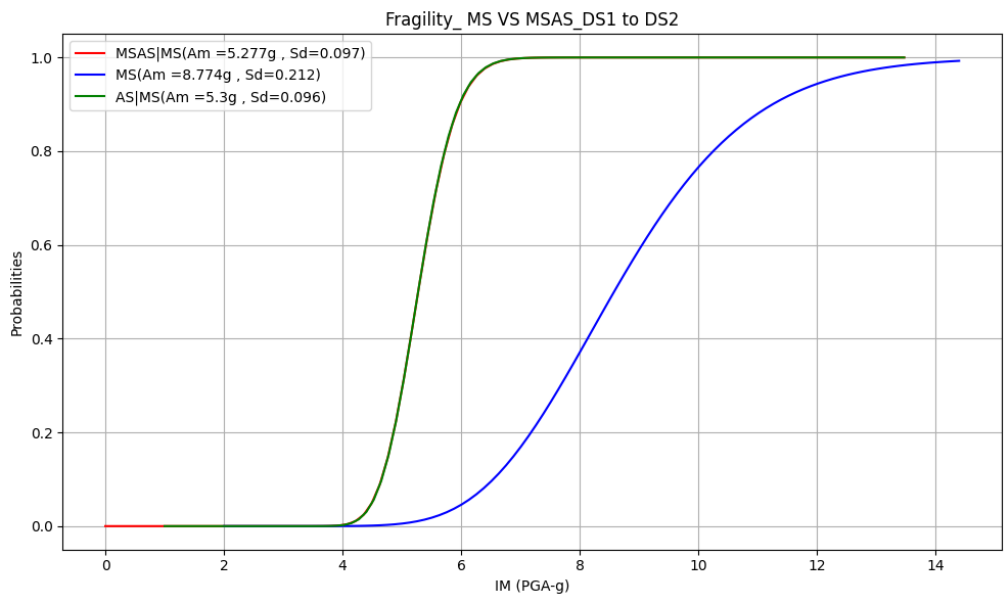


Figure 21 – Comparison of DGB fragility curves: p_{MS} , $p_{AS|MS}$ and $p_{MSAS|MS}$ for DS2.



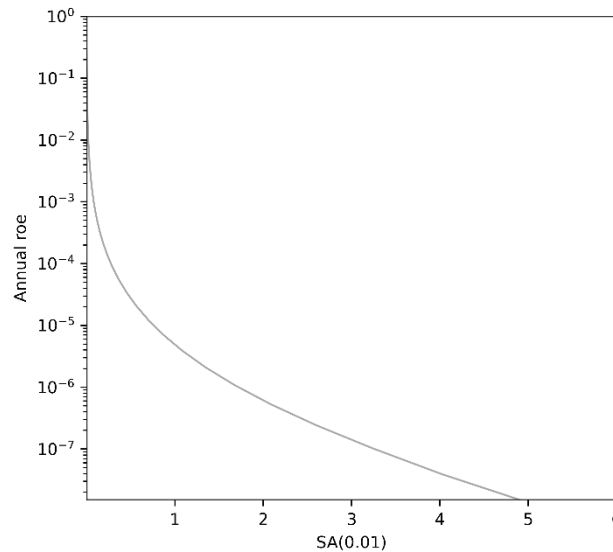


Figure 22 – Hazard curve for METIS case study

2.3. Sensitivity analysis

2.3.1. Case study: Water pump

To assess the behavior of the damaged component, in terms of the definition of the intermediate damage and collapse states, we explored setting different ductility values for Water pump and deriving the fragility curves for each case. Here, we repeated the fit of the damage-state-dependent and intact fragility curves for three different collapse ductility values: the original value of $\mu=1.25$, the value of $\mu=2.5$ considered in the previous section, and finally a case with $\mu=4$. Additionally, we also tested changing the intermediate damage state (DS1) threshold to explore the impact on the fragility curves with respect to the MS-only case.

Figure shows the results of this analysis, with each column representing a different collapse value (μ equal to 1.25, 2.5, and 4.0), and each row representing different threshold of DS1. In the top row the onset of DS1 is at a ductility of 1, as originally defined, and in the second row at a ductility of 1.5.

The results in the first row of Figure 23 show, as expected, that increasing the collapse ductility significantly decreases the loss of median capacity when the initial state of the structure goes from DS0 to DS1. This happens because when the threshold of the DS1 and the threshold of collapse are close, then the residual capacity left in the structure already in DS1 after the MS is limited and even a weaker AS would bring it to collapse. This reasoning is confirmed by inspecting the results in the second row when the thresholds between the two damage states are made closer not by increasing the collapse capacity but by increasing the onset of DS1. Again, when the difference between the onset of both damage states is smaller, the reduction in capacity in the fragility curve conditioned to DS1 is more significant.

This sensitivity exercise makes apparent that specific data needs to be gathered on the onset of intermediate damage states of components so that their fragility can be evaluated confidently. Regardless of the definition of intermediate damage states and, therefore, of the characterization of the damage-state-dependent fragility curves, an increase in risk due to the heightened hazard after the MS is to be expected.

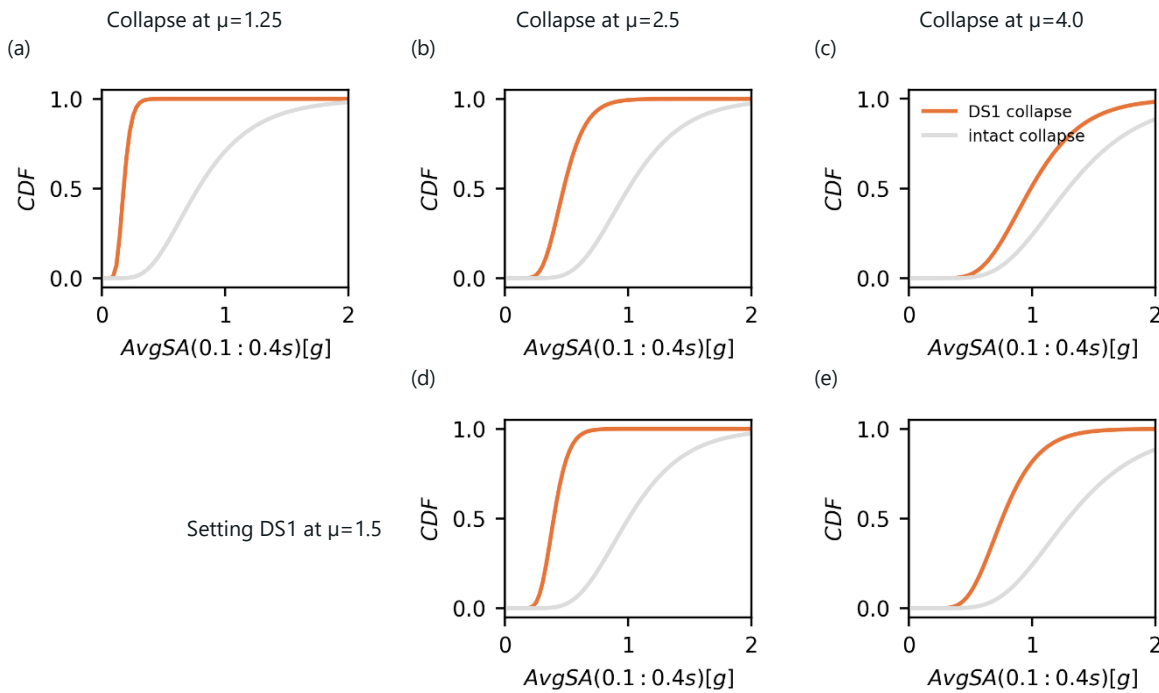


Figure 23 – Sensitivity analysis fragility curves resulting of changing the collapse threshold

3. Practical recommendations for MS-only fragility assessment

Running numerous nonlinear response history analyses for the derivation of fragility curves can be computationally very demanding, particularly in cases when one has complex numerical models. The following subsections detail a set of tests and methods done to determine the most optimal number of records one should run per intensity level (stripe) and the best way to determine at which stripes, in the MSA framework, these analyses should be conducted.

3.1. Determining the number of ground motions per stripe

Generally speaking, the number of *GMs* used in the structural analysis varies from study to study, and it depends on the methodology used to obtain data points (Cloud, *IDA*, *MSA*), the way records are selected, conditioning *IM*, chosen *EDP*, level of the hazard at the site of interest, etc. Our goal here is to provide engineers with recommendations on the number of records to be used in *CS* – based *MSA* scheme when performing a seismic risk assessment. To that end, we look at the response of SDOFs with a fundamental period of 0.1s and 1.0s. The response is estimated using hazard consistent record selection (via *CS*) and multiple stripe analysis (*MSA*), and focuses on the epistemic uncertainty in fragility function parameters (i.e. mean and standard deviation) and in the seismic hazard demand, associated with the finite number of seismic response analyses performed at each *IM* level.

3.1.1. Selection of the ground motions

As a preliminary case study, we use two SDOFs with a vibration period of 0.1s and 1.0s, and with two constitutive models: elastic with hardening and modified Ibarra-Medina-Krawinkler Deterioration Model with Peak-Oriented Hysteretic Response (ModIMKP) (Ibarra et al., 2005). We assume that the SDOFs are located in Perugia, Italy, on a site with $V_{s30}=800\text{m/s}$. We define ten *IMLs* (Table 5), and for each *IML* we select ground motions three times, using *CS* and $S_a(0.1\text{s})$, $S_a(1.0\text{s})$ and $AvgS_a[0.1:2.0:0.1]$, as conditioning *IMs*. To achieve a good fit to the *CS*, the maximum scaling factor used is 6 for the first seven *IMLs* and 10 for the last three *IMLs*, while the minimum considered V_{s30} is 400 m/s. We define



six groups with varying numbers of selected GMs: 3, 7, 11, 16, 22, and 44. To measure the statistical variability of the estimates, we repeat the selection 20 times for each group and every *IML*, every time disregarding part of the selected ground motions - for the case of N3, one record is omitted in each iteration; for N7, three records; for N11, 4 records; for N16, 5 records; for N22, 7 records; and for N44, 11 records.

IML	Return period	poe in 50 years [%]	<i>Sa</i> (0.1s)	<i>Sa</i> (1.0s)	<i>AvgSa</i>
1	42	70	0.2	0.042	0.040
2	72	50	0.26	0.057	0.053
3	140	30	0.35	0.08	0.075
4	475	10	0.58	0.146	0.136
5	975	5	0.78	0.203	0.190
6	2475	2	1.12	0.305	0.285
7	3310	1.5	1.25	0.343	0.320
8	4975	1	1.44	0.402	0.375
9	8310	0.6	1.71	0.485	0.450
10	24975	0.2	2.12	0.697	0.635

Table 5 – Intensity levels and conditioning IMs

In Figure , you can see *SSE_s*, the error metric used to measure the misfit of the selected set to the target distribution, for each group defined and for three *IMLs*. The scatter points refer to the 20 iterations conducted, while the dashed line refers to the *SSE_s* of 0.12 which is considered as the threshold below which the fit is accurate. Across all conditioning *IMs*, group N3 exceeds the acceptable threshold for all intensity levels, while group N7 fluctuates around the threshold. The last four groups have *SSE_s* values below the critical *IML* threshold for the case when *Sa*(1s) and *AvgSa* are used as the conditioning *IMs* and the first 9 *IMLs*. For the last *IML*, group N44 is above the threshold in a few iterations (likely due to the lack of records left in the database as the number of iterations is increasing). Similar behavior is observed for the case when *Sa*(0.1s) is used with the exception that even for the *IML9* there are some iterations for the case of N44 above the acceptable threshold.

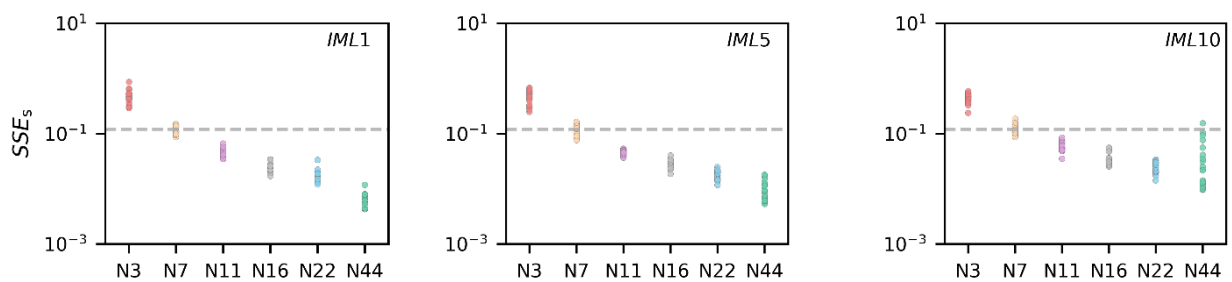


Figure 24 – SSEs obtained for the three different IMLs using *Sa*(1s) as an IM

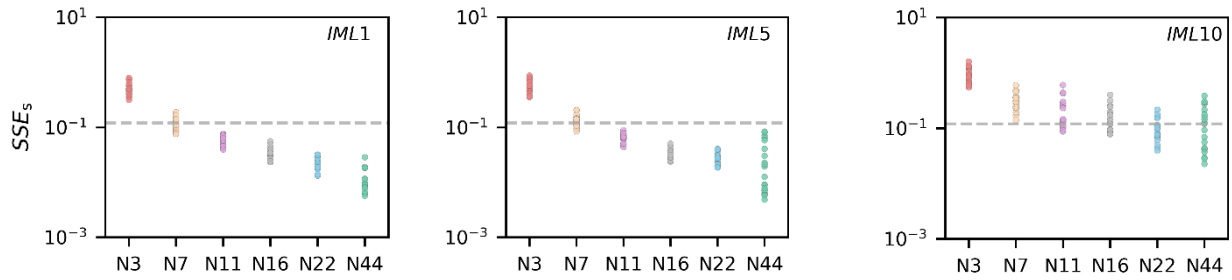


Figure 25 – SSEs obtained for the three different IMLs using $S_a(0.1s)$ as an IM

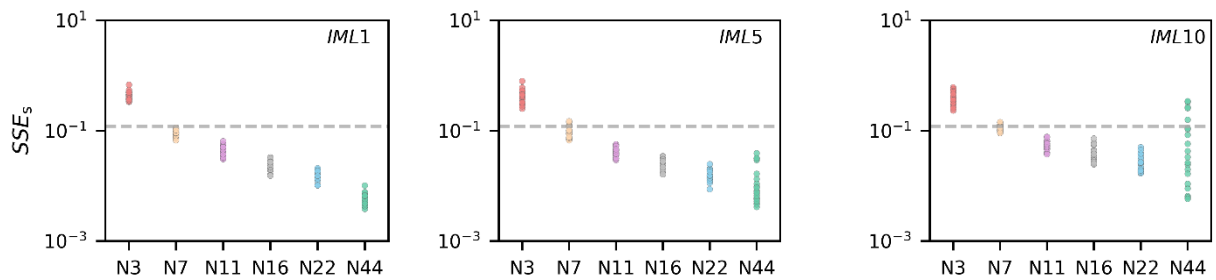


Figure 26 – SSEs obtained for the three different IMLs using $AvgS_a$ as an IM

3.1.2. Computation of the fragility curves

To derive the fragility curves, we run the NLRHA for each *IML* and each group using 20 selected sets of records. For instance, for the N3 group, we performed 600 runs by running three ground motions for 10 IMLs 20 times (as we have 20 iterations). We define three damage states using ductility levels $\mu = 2, 3,$ and 6 as onset values of the minor, moderate, and total damage states. In Figure one can see the monotonic backbone curve for the ModIMKP constitutive law with the damage states indicated.

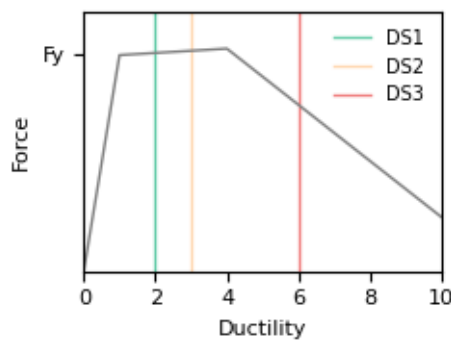


Figure 27 – Monotonic backbone of the ModIMKP material model with damage states indicated

We derive fragility functions for every group by assuming lognormal distribution and using the maximum likelihood method (Baker, 2015). Just by visual inspection, we can see that the variability in the fragility curves is lower when we have more records (we show here only the case of $S_a(0.1s)$) but the same

trend is observed for $Sa(1.0s)$ and $AvgSa$. This trend is not as apparent for the lower ductility levels as it is for the $\mu = 6$ (collapse).

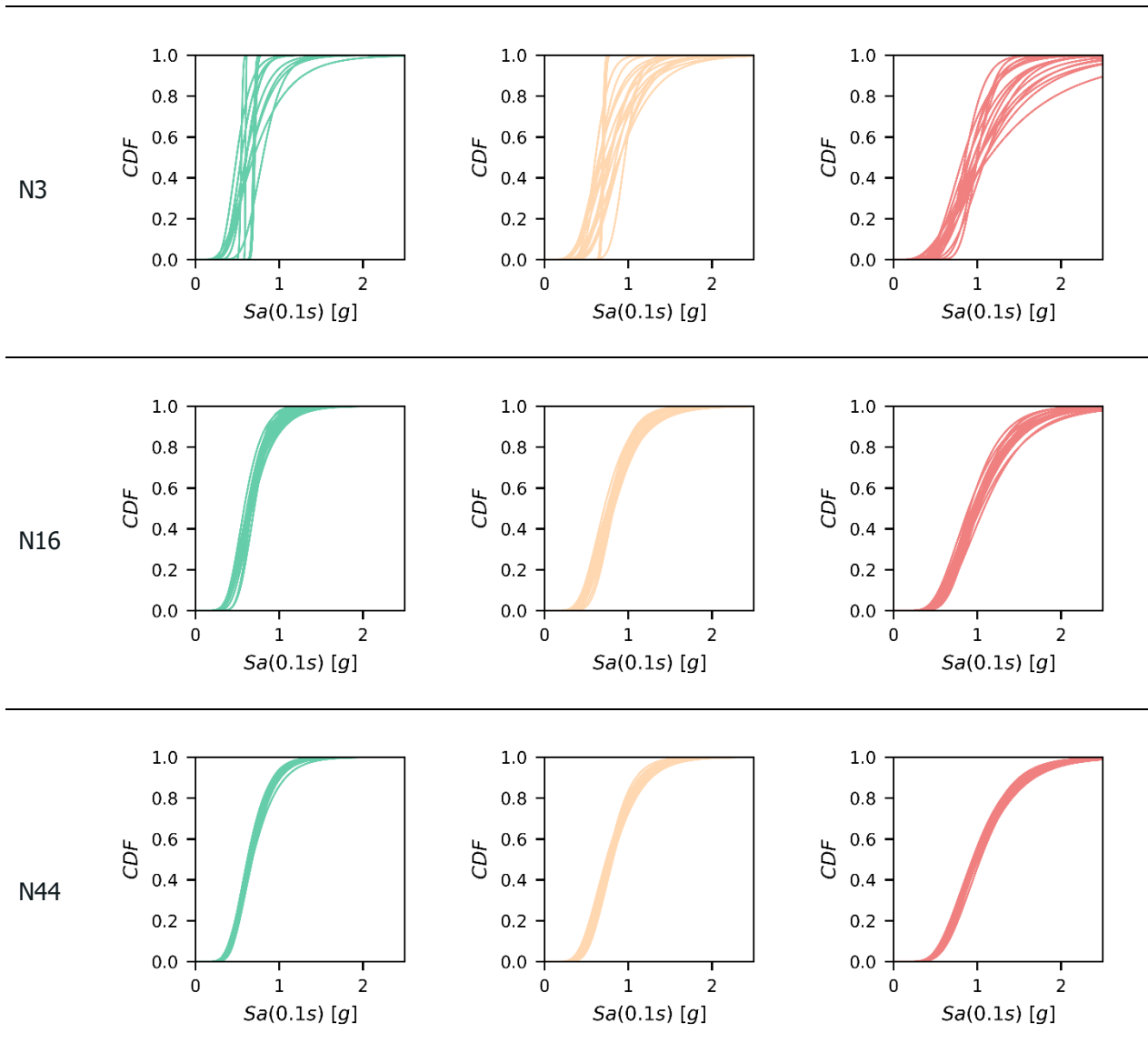


Figure 28 – Fragility curves obtained with 20 ground motion sets for three damage states ($\mu = 2, 3$ and 6 , from left to right). The figure shows the results for SDOF with $T_1 = 0.1s$ and $Sa(0.1s)$ as conditioning IM.

Figure shows the distribution of the median and standard deviation of the fragility functions for every group considered (and for ModIMKP model). To estimate the epistemic uncertainties associated with the fragility function parameters, we found the coefficient of variation (COV) for both median and standard deviation reported in Table 6 for the case of $Sa(0.1s)$ and ModIMKP material model. The COV of the standard deviation is much larger than the one of the median, which is not surprising. Also, as expected, by increasing the number of records the COV decreases. Similar results are obtained for all conditioning IMs and both constitutive models. The COV of the median of the fragility curves is below 10% for all cases considered if there are at least 7 records per stripe. The results for the 1s SDOF system, not shown here, are similar to those above.

(a)

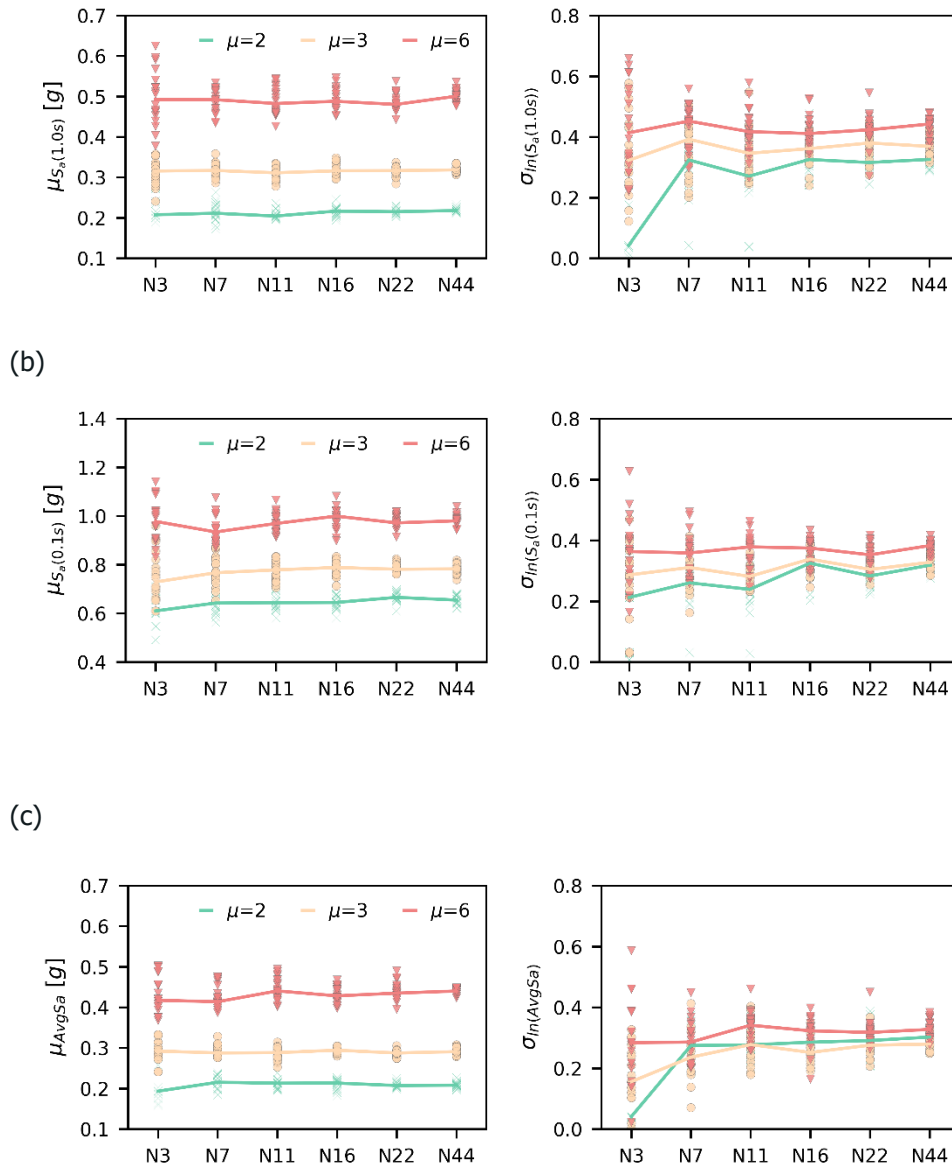


Figure 29 – Estimates of the fragility function parameters. Scatter points refer to 20 different iterations while solid lines connect the median values. Note: This figure shows the results obtained for the dynamic analysis of an SDOF with ModIMKP material model and $T_1=0.1s$.

	N3	N7	N11	N16	N22	N44
$\mu = 2$	0.11/0.66	0.06/0.26	0.06/0.29	0.04/0.13	0.03/0.12	0.03/0.06
$\mu = 3$	0.14/0.47	0.08/0.19	0.05/0.16	0.04/0.12	0.02/0.09	0.02/0.08
$\mu = 6$	0.08/0.3	0.06/0.19	0.04/0.16	0.04/0.1	0.03/0.11	0.02/0.05

Table 6 – COV in the fragility curve parameter estimates (median/ standard deviation). Note: This table shows the results obtained for the dynamic analysis of an SDOF with ModIMKP material and $T_1=0.1s$.

D6.7 Influence of aftershocks and clustered seismicity on seismic fragility

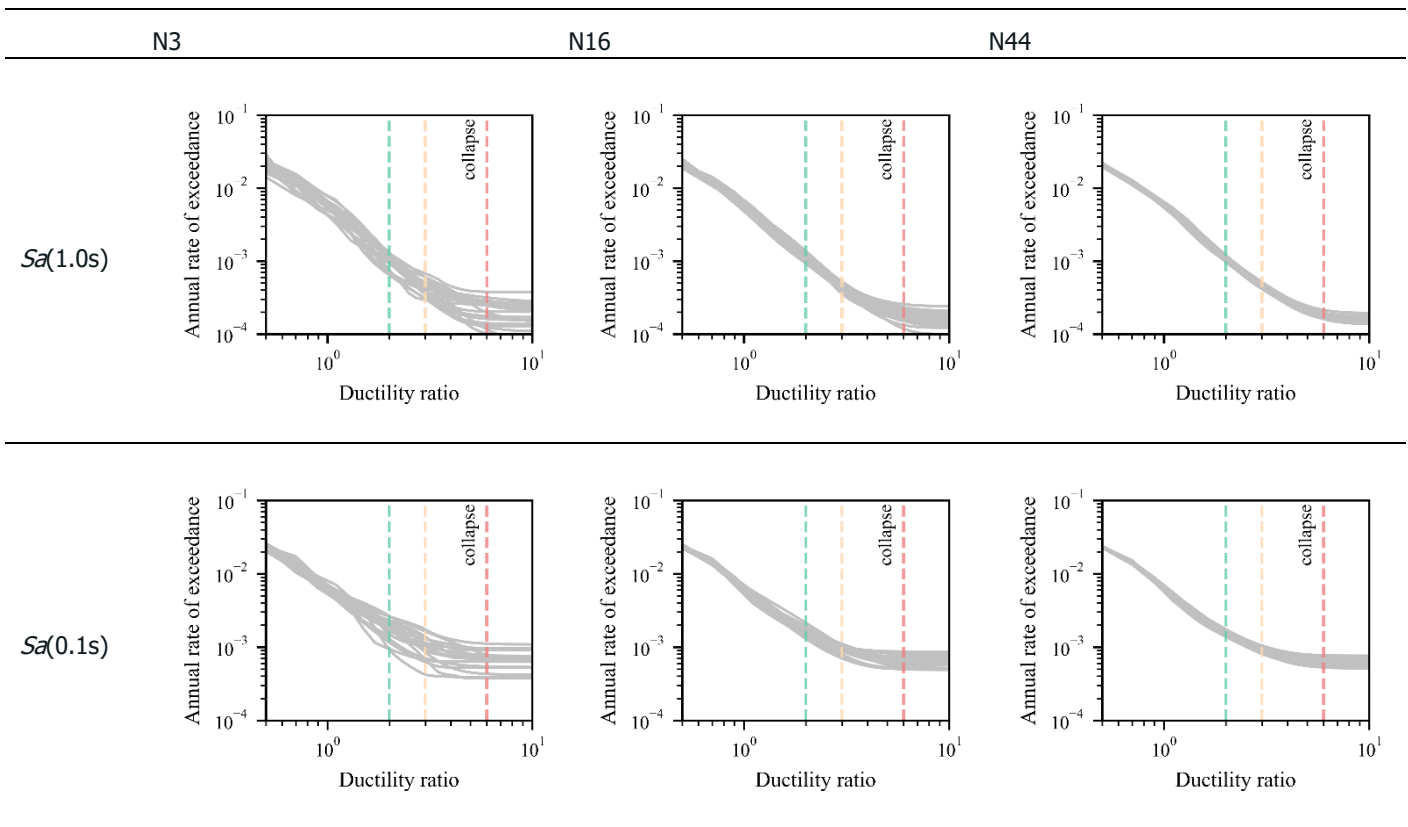


Lastly, we use the obtained results to derive the seismic demand hazard curves for both SDOF systems. Seismic demand hazard, which represents the rate of exceeding a specific EDP level in a given period of time, such as one year, is a metric commonly used to quantify the seismic performance of a structure. It can be calculated by combining the probability of exceeding the specific demand level $EDP=edp$ due to the ground motion intensity $P(EDP>edp|IM=im)$ with the rate of “equaling” ground motion intensity IM (λ_{IM}). Following Shome and Cornell $P(EDP>edp|IM=im)$ can be separated into the mutually exclusive events of collapse and non-collapse, yielding the following expression:

$$\lambda_{EDP}(edp) = \int_0^{+\infty} [P(EDP > edp|\bar{C}, IM = im)(1 - P_{col}) + P_{col}] |d\lambda_{IM}(im)| \quad (3)$$

Maximum likelihood method (Baker, 2015) was used to compute the probability of collapse for each intensity level while $P(EDP>edp|\bar{C}, IM=im)$ was modeled using linear regression. $\lambda_{IM}(im)$ is the annual rate of IM exceeding im level.

By calculating the λ_{EDP} for a range of edp response values we obtain the response hazard curve. In Figure 23, we show the response hazard curves cast in terms of ductility ratio for different sets of records. Similarly as in the case of fragility functions, the variability reduces as we increase the number of records used. When it comes to the mean seismic demand hazard curves, as seen in Figure , there is almost no apparent difference between the curves obtained with the different groups of records. However, as illustrated in Figure the COV of the estimated exceedance rates increases, as expected, for the higher ductilities and decreases as we utilize more records. For the first two damage states the COV is below 15% if we use at least 11 records per stripe while for the last damage states at least 22 records are needed to achieve the same accuracy.



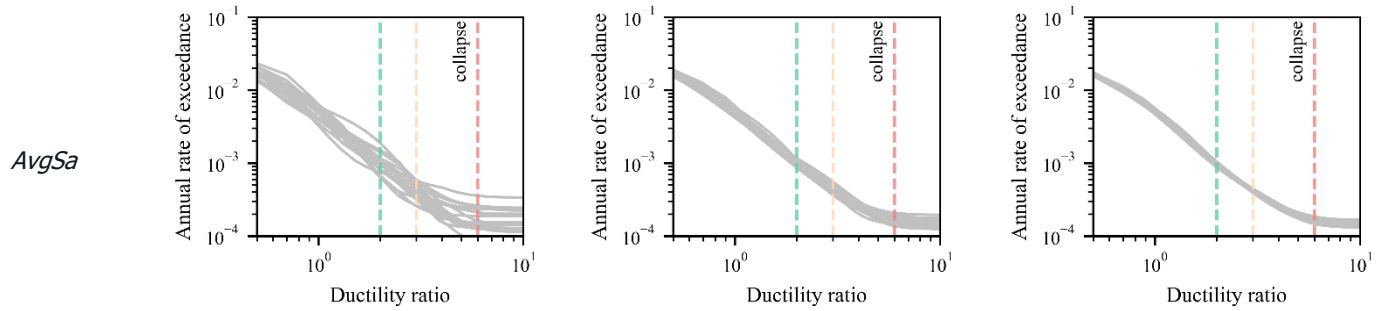


Figure 30 – Ductility hazard curves obtained for sets of ground motion records with different number of accelerograms (from 3 to 44). Each panel shows curves from 20 different ground motions sets. Note: This figure shows the results obtained for the dynamic analysis of a SDOF with ModIMKP material model.

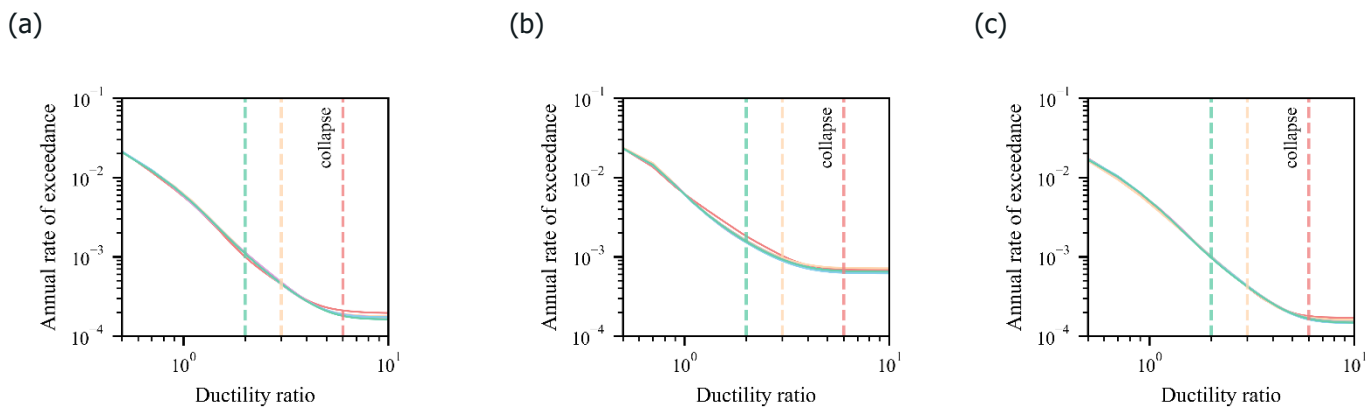


Figure 31 – Comparison of mean response hazard curves using different record selection variants in terms of ductility ratio and: (a) $S_a(T=1s)$, (b) $S_a(T=0.1s)$ and (c) AvgSa as a conditioning IM. Note: This figure shows the results obtained for the dynamic analysis of a SDOF with ModIMKP material mode.

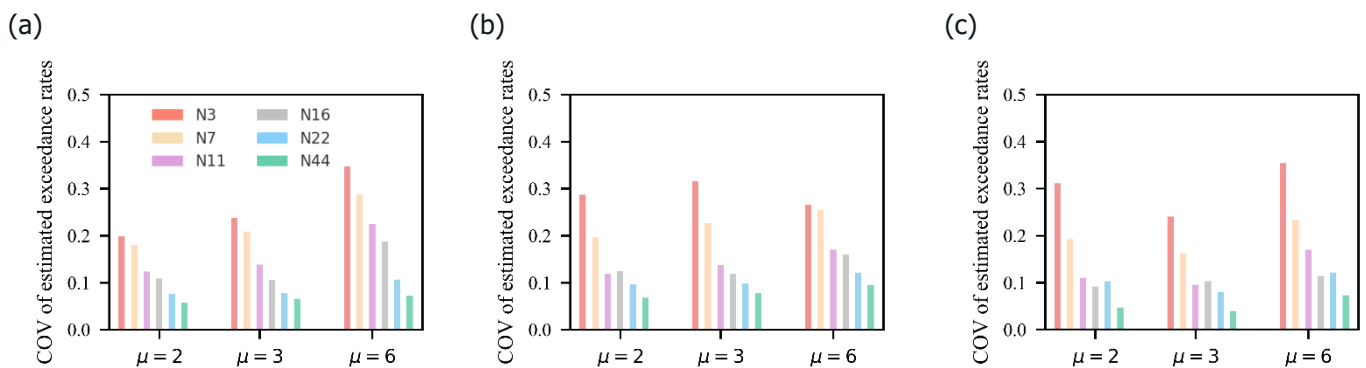


Figure 32 – COV of estimated exceedance rates at different ductility levels and for different record sets: (a) $S_a(1s)$, (b) $S_a(0.1s)$ and (c) AvgSa. Note: This figure shows the results obtained for the dynamic analysis of a 0.1s SDOF with ModIMKP material model.



3.2. Determination of the number of stripes for MSA

Within the MSA framework, the NLRHA results across various IMLs, or stripes, serve as the basis for estimating the median and dispersion of the fragility curve through a maximum likelihood approach. This section aims to pinpoint the specific stripes for analysis and determine the necessary levels for obtaining reliable fragility estimates.

Building upon the insights from the previous section, we maintain a consistent number of records in each stripe. However, we acknowledge that a more refined approach would involve simultaneously adjusting both the record count per stripe and selecting relevant stripes. Despite this, we contend that these adjustments would have a relatively minor impact, influencing the probability of exceedance within a stripe to a small extent. On the contrary, introducing a new stripe significantly affects fragility behavior.

To efficiently identify the optimal intensity levels for analysis, we employ Bayesian updating, a statistical method allowing us to update the probability distribution as new information emerges, utilizing Bayes' theorem:

$$p_D(\theta|D) = \frac{p(D|\theta)p_0(\theta)}{p(D)} \quad (4)$$

Where $p_D(\theta|D)$ is the posterior (updated distribution) of the unknown parameters θ given the data D . In our case, we are interested in updating the distribution of the median μ and standard deviation σ of the fragility curve, $\theta = [\mu, \sigma]$. The new data D is obtained analytically, from the results of the NLRHA. The term $p_0(\theta)$ refers to the initial ('prior') joint probability distribution of θ , $p(D|\theta)$ is the probability of obtaining the data D given the parameters θ (known as the likelihood function) and $p(D)$ is the marginal distribution of data D . The likelihood function is defined assuming that at each IML_j level, the probability of observing z_j collapses out of n_j ground motions with IML_j is well represented with the binomial distribution. Calculating $p(D)$ often involves complex analytical integration over all possible values of θ . To address this challenge, the Markov chain Monte Carlo (MCMC) statistical model is employed, coupled with the Metropolis-Hastings algorithm. This approach eliminates the need to compute a normalizing term. The underlying principle of MCMC involves simulating a random walk in the parameter space, drawing samples from an assumed distribution. This walk gradually converges to a stationary distribution. The term Markov chain in MCMC refers to the fact that the samples are drawn sequentially, i.e., they depend on the samples drawn in the previous iteration, in that way Markov chain, which presents the chain of random variables, is made (Gelman et al., 2003). After sampling, the draws are corrected to better approximate the target posterior distribution (i.e., $p_D(\theta|D)$), in this way the approximate distributions are improved at each iteration, converging to the target distribution. To this aim, we use Metropolis – Hasting algorithm, which in some cases accepts and in others rejects the drawn samples based on a set of criteria. Other techniques such as Gibbs sampler, slice sampling, and perfect sampling can be used (Robert and Casella, 2013). The process of Bayesian updating is done following the steps described below:

1. First, we assume the distribution of the unknown parameters (μ and σ) – in this case, both the mean and standard deviation of the fragility function are modeled as lognormally distributed variables with some mean and standard deviation.
2. Define the prior values of θ - mean and standard deviation of μ and σ .
3. Initialize the algorithm at some position in parameter space $\theta_{current}$. This position is chosen arbitrarily but reasonably. These values do not affect the final results but they might affect the speed at which we come to the stationary result.
4. Define the 'new data' to feed the model. In this case, these are the results of the numerical simulations.
5. Calculate the posterior joint probability distribution of the current parameters
6. Define the number of runs. In this case, 10000 simulations, as it seemed to be sufficient. For every run k :
 - a. Propose a jump to a new position in the parameter space – θ_{new} using a proposal (or jumping) distribution – $T(\theta_t|\theta_{t-1})$. Here, we used a normal distribution with the mean of the current mean and standard deviation of 0.5 to jump to a new position in the parameter space.



- b. Calculate the joint probability distribution of the proposed parameters similar to what is described in Step 5.
- c. Find the acceptance probability which is defined as the minimum of 1 and the ratio of the distributions found in Step 6b and Step 5:

$$r = \min \left\{ \frac{p_0(\theta_{new}) * p(D|\theta_{new})}{p_0(\theta_{current}) * p(D|\theta_{current})}, 1 \right\} \quad (5)$$

- d. Draw the random number u from the uniform distribution in range (0, 1). Set:

$$\theta_{current} = \begin{cases} \theta_{new}, & \text{if } r > u \\ \theta_{current}, & \text{otherwise} \end{cases} \quad (6)$$

7. Once Step 6 is performed for each iteration we can investigate the convergence of the algorithm.
8. Finally, we can estimate the final posterior distribution of μ and σ . We find these values by taking the mean of all of the samples.

The process of Bayesian updating begins with establishing a reasonable prior distribution, which can be derived from various sources depending on the specific structure or component of interest. Approaches such as simplified analysis (e.g., EPRI (2018)), nonlinear static analysis (SPO2FRAG [Blatzopoulos et al., 2017]), or the use of UHS (NUREG-0800 (2014)) are viable methods for defining the prior. Once the prior is defined, it is updated with new data, such as the addition of a new stripe in our case. The process starts with two stripes, and the fragility is updated according to the described procedure. Subsequently, the updated prior becomes the new posterior, which then prompts the need to determine the next stripe for analysis. To guide this decision, we utilize the method outlined in Jalayer (2003), which involves fitting a linear regression model in log EDP-IM space based on the existing stripes. This model predicts the structure's response on other stripes in terms of median and standard deviation. The following steps provide a detailed outline of this process:

1. Define an initial fragility curve as prior.
2. Run time history analysis for two stripes, using the fixed number of records. These stripes are recommended as those with an IML near the median capacity of the original fragility, and the other one should have a lower intensity.
3. Perform the first updating of the parameters.
4. To define the next stripe, perform linear regression on the known stripes and predict all unknown k possible stripes (out of a predefined set of IML).
 - a. Based on the interpolated mean and standard deviation of the response, obtain the probability of exceedance of the limit state.
 - b. Perform k updates, using the current prior and the new stripe's probability of exceedance.
 - c. Compare which k stripe produces the largest change in fragility between prior and k posterior, which will become the next stripe.
5. Perform the real updating using this new stripe IML, with the results from the NLRHA.
6. We repeat the process (steps 4 and 5) until the change between prior and posterior becomes negligible. This change is measured through the value of the Kolmogorov–Smirnov (KS, 1951) statistic shown in Equation (6).

$$D_{KS} = \sum |F(x)_{prior} - G(x)_{posterior}| \quad (7)$$

In the described methodology, in step 4, as shown in Figure , the left panel illustrates the response on the three known stripes using the conducted analysis. Based on this data, a linear regression is performed to predict the response on the remaining stripes. Using the predicted values, the methodology determines which stripe would cause the most significant change in the fragility. In the specific case mentioned, the selected stripe corresponds to an *IML* of 0.9g. Subsequently, the analysis is carried out on this selected stripe, which then becomes the 'known stripe,' as depicted on the right panel of Figure . This process is repeated iteratively, with each new stripe becoming the 'known stripe' for the subsequent round of analysis and prediction.



With each iteration, the interpolation in step 4 improves as more data points are gathered in the *EDP-IM* space. Initially, the interpolation may choose a point relatively far from the previous iterations, as illustrated when it selected the penultimate stripe. However, as more information becomes available, the interpolation tends to gravitate toward the central stripes, allowing for better adjustment of the curve. This adaptive behavior essentially results in the automatic selection of the stripe that has the most influence on the final outcome. As the iterations progress, it becomes possible to observe when the changes in the interpolated curve become less substantial, signaling that the analysis is approaching a point close to the benchmark or a stable solution.

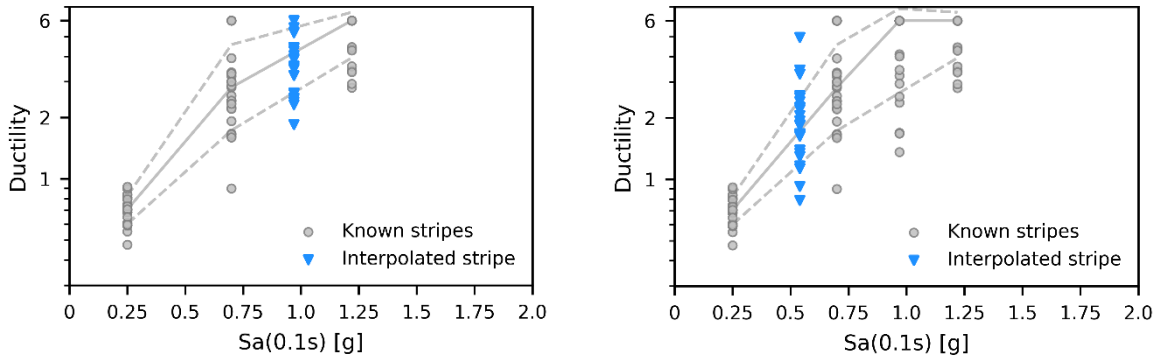
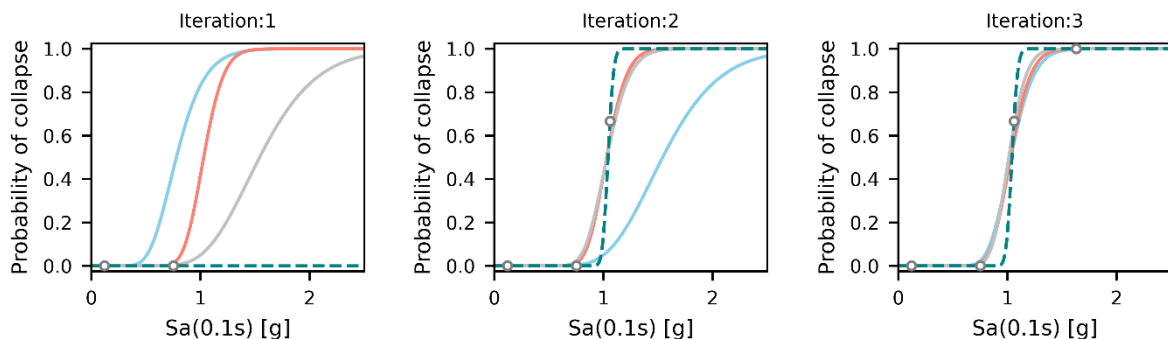


Figure 32 - Example of interpolation to obtain the expected response for new IML

3.2.1. Case study SSC: Service water pump

The reactor and pump are assumed to be situated in Tuscany, Italy, on rock with a V_{s30} value of 1000 m/s. PSHA calculations are conducted using OpenQuake software (Pagani et al., 2014) and the area source model based on the European Seismic Hazard Model (ESHM20). The hazard analysis employs a logic tree with five branching sets, each with three branches, resulting in a total of 125 distinct paths. Two ground motion models (GMMs) are employed, each with equal weights of 0.5: one from (Kotha et al., 2020) adapted by (Weatherill et al., 2020), and the other from (Lanzano et al., 2022). To establish the benchmark fragility curve, 43 ground motions at ten IMLs corresponding to return periods from 475 to 100,000 years are selected. The initial prior distribution of the fragility curve is derived from the EPRI (2018) approach, based on the pump's design values associated with the Uniform Hazard Spectrum (UHS). This methodology incorporates various factors detailed within the guidelines to determine an expected collapse fragility curve. For this specific pump, the prior parameters are set as: $\mu=0.78g$ and $\sigma=0.26$. These parameters are depicted as the blue line (prior) for iteration 1 in Figure . Building upon the insights from the previous section, the number of analyses per stripe is fixed at 15.



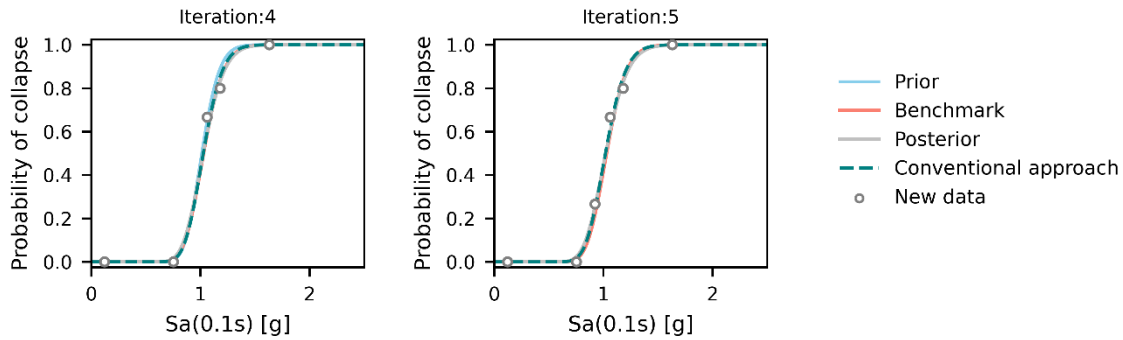


Figure 33 - Fragility curves per iteration, showing normal fit (with considered data) and Bayesian procedure

Figure illustrates the results of the analysis after five iterations, involving a total of 6 stripes out of the 10 used for the benchmark, with a reduced number of records. The fragility curve obtained with Bayesian updating is compared with the one obtained without Bayesian updating (referred to as the 'conventional approach'), where μ and σ are estimated with maximum likelihood using the available stripes, as well as with the benchmark. It is evident that even after the second iteration, the fragility curve obtained with Bayesian updating approaches the target median and dispersion of 1.03g and 0.14, respectively. Despite the initial prior, derived from EPRI, having a different median and dispersion, the new data points facilitated a quick convergence towards the actual solution. The results demonstrate that the method applied enables the automatic selection of the next stripe, leading to rapid convergence, within only a few iterations, to the benchmark. Furthermore, Figure illustrates that the conventional approach of fitting using only the available stripes may require more analysis to converge to the benchmark. This indicates that in this case, utilizing this methodology can help reduce the number of analyses required to estimate the fragility of SSCs, thereby reducing computational costs.

4. Conclusions and Recommendations

This report focused on the development of hazard consistent fragility curves for clustered seismicity. These curves, called damage-dependent, are derived through numerical analyses of ground motions for seismic sequences and require the definition of at least one intermediate damage state between the intact condition and collapse.

Having selected hazard consistent MS and AS ground motions for the METIS site, it was possible to conduct back-to-back response analysis, monitoring the levels of damage after each MS and AS signal. We derived the fragility curves by classifying the responses after the MS and using cloud analysis to obtain the fragility parameters. This methodology was applied to a service water pump, mounted on a reactor building model, and by assuming an intermediate damage state (DS1) once the structure becomes nonlinear.

The results show a loss of median capacity, with respect to the intact case, the amount of which depends on the definition of the collapse and DS1 thresholds. These thresholds were modified in a sensitivity analysis scheme to assess the impact of their definition on the loss of median capacity. The findings showed, as expected, that the closer the threshold of both damage states the larger the loss in median capacity. If the onset of the intermediate damage is far from the onset of the collapse state, then the relatively minor amount of structural damage does not affect much the median residual capacity at collapse. This methodology could be improved and complemented with a more in-depth look at the damage mechanisms of the structures and components present on NPPs, allowing for a more accurate estimation of the intermediate levels of damage, as well as the calibration of different damage metrics, similar to the work done in Iñarritu et al (2024).

To conclude the proposed methodology for the derivation of damage-state-dependent fragility curves is statistically robust and scientifically well grounded. However, it requires running a large number of analyses, a task that may be challenging especially if the FEM model of the structure is complex.



Therefore, before embarking in such an endeavor a careful evaluation of whether the aftershock pose a significant threat to the integrity of SSC should be conducted first using simplified models.

Along these lines, this report includes some practical recommendations related to how to use judiciously the number of analyses that one is willing to consider obtaining fragility curves under the MSA framework. To do so, we first investigated how the number of ground motions per stripe affects the match to the target conditional spectrum and the resulting fragility curve. We showed that to get a good match to the target more than 7 records per stripe are recommended while to have stable median and dispersion estimates of the fragility curve at least 11 or 16 ground motions are needed, depending on the desired level of accuracy.

Next, we introduced a Bayesian updating methodology designed to optimize the selection of stripes and the number of stripes needed to produce reliable results. The methodology was tested on a service water pump, located on AP1000 reactor building, placed on the METIS case study site. The results highlighted the significant potential for reducing the number of analyses with this proposed approach without compromising the accuracy of the fragility curve.

Results presented here showed that the use of Bayesian updating, paired with an algorithm that allows us to measure the possible impact of a new stripe of data, can help optimize and automate the number of NLRHA required to obtain an SSC fragility curves within a desired level of error tolerance. The introduction of Bayesian Updating leads to a faster convergence when compared to conventional fitting of the data through the maximum likelihood based only on the analysed stripes. This methodology may also identify once convergence is achieved as the stripes providing the largest differences between iterations are always selected, meaning that once the differences between two consecutive iterations of fragility curves become small, then the curve's parameters have achieved statistically robust values. Future improvements for this work may involve the introduction of multiple damage states, as well as the consideration of a variable number of records per stripe, aiming to further reduce the number of required analyses. Additionally, the stopping criteria, which is currently based on the difference between each iteration and the next across all IM values, may also be modified. This modification could give additional or higher weights according to the higher relevance one could assign to the lower IM values which are related to higher rates and therefore may control the risk results. Finally, some combination and improvement to this approach may deal with simultaneous optimization of both the number of records per stripe and their position, to further minimize the computational efforts.

5. Acknowledgements

We would like to thank Mohamed Zouatine for creating the structural model of the diesel generator building in OpenSees.

6. Bibliography

ASCE, 2000. Prestandard and Commentary for the Seismic Rehabilitation of Buildings, FEMA 356 Report, prepared by the American Society of Civil Engineers for the Federal Emergency Management Agency, Washington, D.C.

Baker, J. W., 2011. Conditional mean spectrum: Tool for ground-motion selection. *Journal of Structural Engineering*, 137(3), 322–331. DOI: 10.1061/(ASCE)ST.1943-541X.0000215

Baker, J. W., 2015. Efficient analytical fragility function fitting using dynamic structural analysis. *Earthquake Spectra*, 31(1), 579–599. DOI: 10.1193/021113EQS025M

Baltzopoulos, G., Baraschino, R., and Iervolino, I., 2019. On the number of records for structural risk estimation in PBEE. *Earthquake Engineering and Structural Dynamics*, 48(5), 489–506. DOI: 10.1002/eqe.3145

Baltzopoulos, G., Baraschino, R., Iervolino, I., and Vamvatsikos, D., 2017. SPO2FRAG: software for seismic fragility assessment based on static pushover. *Bulletin of Earthquake Engineering*, 15(10), 4399–4425. Springer Netherlands. DOI: 10.1007/s10518-017-0145-3

D6.7 Influence of aftershocks and clustered seismicity on seismic fragility



Baraschino, R., Baltzopoulos, G., & Iervolino, I. (2023). A note on peak inelastic displacement as a proxy for structural damage in seismic sequences. *Procedia Structural Integrity*, 44, 75-82.

Boore, D. M., and Atkinson, G. M., 2008. Ground-motion prediction equations for the average horizontal component of PGA, PGV, and 5%-damped PSA at spectral periods between 0.01 s and 10.0 s. *Earthquake Spectra*, 24(1), 99–138. DOI: 10.1193/1.2830434

Bradley, B. A., 2010. A generalized conditional intensity measure approach and holistic ground-motion selection, (February), 1321–1342. DOI: 10.1002/eqe

Bradley, B. A., 2013. Practice-oriented estimation of the seismic demand hazard using ground motions at few intensity levels, (June), 2167–2185. DOI: 10.1002/eqe

Cordova, P. P., Deierlein, G., Mehanny, S. S. F., and Cornell, C. A., 2001. Development of a two-parameter seismic intensity measure and probabilistic design procedure. *Journal of Engineering and Applied Science*, 51(2), 233–252.

Cornell, C.A., Jalayer, F., Hamburger, R.O. and Foutch, D.A., 2002. Probabilistic basis for 2000 SAC federal emergency management agency steel moment frame guidelines. *Journal of structural engineering*, 128(4), pp.526-533.

Eads, L., Miranda, E., Krawinkler, H., and Lignos, D. G., 2012. An efficient method for estimating the collapse risk of structures in seismic regions. DOI: 10.1002/eqe

EPRI, 2018. Seismic Fragility and Seismic Margin Guidance for Seismic Probabilistic Risk Assessments, Technical Report, Electric Power Research Institute EPRI. Palo Alto, CA.

FEMA P-58, 2012. Federal Emergency Management Agency: Seismic Performance Assessment of Buildings, prepared by the Applied Technology Council for the Federal Emergency Management Agency. Washington, D.C.

FEMA 440, 2005. Federal Emergency Management Agency: Improvement of Nonlinear Static Seismic Analysis Procedures, prepared by ATC-55 Project for the Federal Emergency Management Agency. Washington, D.C.

Gelman, A., Carlin, J. B., Stern, H. S., Dunson, D. B., Vehtari, A., and Rubin, D. B., 2003. *Bayesian Data Analysis - 2nd edition*. Chapman & Hall/CRC Texts in Statistical Science Series. DOI: 10.4135/9781071812082.n42

Ibarra, L. F., Medina, R. A., and Krawinkler, H., 2005. Hysteretic models that incorporate strength and stiffness deterioration. *Earthquake Engng Struct. Dyn.*, 34(Earthquake Engng Struct. Dyn. 2005; 34), 1489–1511. DOI: 10.1002/eqe.495

Iervolino, I., 2022. Estimation uncertainty for some common seismic fragility curve fitting methods, 152(November 2021).

Inarritu, P. G. de Q., Šipčić, N., Alvarez-Sanchez, L., Kohrangi, M., and Bazzurro, P., 2023. A closer look at hazard- consistent ground motion record selection for building- specific risk assessment: Effect of soil characteristics and accelerograms' scaling. *Earthquake Spectra*, 00(0), 1–38. DOI: 10.1177/87552930231173713

Inarritu, P. G. D. Q., Kohrangi, M., & Bazzurro, P. (2024). Damage assessment of unreinforced masonry buildings incorporating damage accumulation. *Earthquake Engineering & Structural Dynamics*, 53(6), 2122-2140.

Jalayer, F., 2003. *Direct Probabilistic Seismic Analysis: Implementing Non-Linear Dynamic Assessments*. Stanford University.

Jalayer, F., and Cornell, C. A., 2009. Alternative non-linear demand estimation methods for probability-based seismic assessments. *Earthquake Engineering and Structural Dynamics*, 38(8), 951–972. DOI: 10.1002/eqe.876

D6.7 Influence of aftershocks and clustered seismicity on seismic fragility



- Jayaram, N., Lin, T., and Baker, J. W., 2011. A Computationally efficient ground-motion selection algorithm for matching a target response spectrum mean and variance. *Earthquake Spectra*, 27(3), 797–815. DOI: 10.1193/1.3608002
- Jeon, J.-S., DesRoches, R., Lowes, L. N., & Brilakis, I. (2015). Framework of aftershock fragility assessment-case studies: older California reinforced concrete building frames. *Earthquake Engineering & Structural Dynamics*, 44(15), 2617–2636. <https://doi.org/10.1002/eqe.2599>
- Jeon, J. S., Mangalathu, S., Song, J., and Desroches, R., 2019. Parameterized Seismic Fragility Curves for Curved Multi-frame Concrete Box-Girder Bridges Using Bayesian Parameter Estimation. *Journal of Earthquake Engineering*, 23(6), 954–979. DOI: 10.1080/13632469.2017.1342291
- Kiani, J., Camp, C., and Pezeshk, S., 2018. On the number of required response history analyses. *Bulletin of Earthquake Engineering*, 16(11), 5195–5226. Springer Netherlands. DOI: 10.1007/s10518-018-0381-1
- Kohrangi, M., Bazzurro, P., Vamvatsikos, D., & Spillatura, A. (2017). Conditional spectrum-based ground motion record selection using average spectral acceleration. *EARTHQUAKE ENGINEERING & STRUCTURAL DYNAMICS Earthquake*. <https://doi.org/10.1002/eqe.2876>
- Kotha, S. R., Weatherill, G., Bindi, D., and Cotton, F., 2020. A regionally adaptable ground motion model for shallow crustal earthquakes in Europe. *Bulletin of Earthquake Engineering (Vol. 18)*. Springer Netherlands. DOI: 10.1007/s10518-020-00869-1
- Kwag, S., and Gupta, A., 2018. Computationally efficient fragility assessment using equivalent elastic limit state and Bayesian updating. *Computers and Structures*, 197, 1–11. DOI: 10.1016/j.compstruc.2017.11.011
- Lanzano, G., Felicetta, C., Pacor, F., Spallarossa, D., and Traversa, P., 2022. Generic-To-Reference Rock Scaling Factors for Seismic Ground Motion in Italy. *Bulletin of the Seismological Society of America*, (March). DOI: 10.1785/0120210063
- Massey, F. J. (1951). The Kolmogorov-Smirnov Test for Goodness of Fit. *Journal of the American Statistical Association*, 46(253), 68–78. <https://doi.org/10.2307/2280095>
- McKenna, F., Fenves, G. L, and Scott, M. H. (2000). Open System for Earthquake Engineering Simulation. University of California, Berkeley. <http://opensees.berkeley.edu>.
- NUREG-0800, 1989. U.S. Nuclear Regulatory Commission, Standard Review Plan, Revision 2. Washington, D.C.
- Ogata, Y. (1988). Statistical Models for Earthquake Occurrences and Residual Analysis for Point Processes. *American Statistical Association*, 83(401), 9–27.
- Pagani, M., Monelli, D., Weatherill, G., Danciu, L., Crowley, H., Henshaw, P., Butler, L., Nastasi, M., Panzeri, L., Simionato, M., & Vigano, D. (2014). OpenQuake Engine: An Open Hazard (and Risk) Software for the Global Earthquake Model. *Seismological Research Letters*, 85(3), 692–702. <https://doi.org/10.1785/0220130087>
- Papadopoulos, A. N., Kohrangi, M., & Bazzurro, P. (2019). Correlation of spectral acceleration values of mainshock-aftershock ground motion pairs. *Earthquake Spectra*, 55(1), 39–60. <https://doi.org/10.1193/020518EQS033M>
- Papadopoulos, A. N., Kohrangi, M., & Bazzurro, P. (2020). Mainshock-consistent ground motion record selection for aftershock sequences. January, 754–771. <https://doi.org/10.1002/eqe.3263>
- Park, Y. J., Ang, A. H. S., & Wen, Y. K. (1985). Seismic damage analysis of reinforced concrete buildings. *Journal of Structural Engineering*, 111(4), 740-757.
- Robert, C. P., and Casella, G., 2010. Introducing Monte Carlo Methods with R Solutions to Odd-Numbered Exercises. arXiv: Methodology. Retrieved from <https://api.semanticscholar.org/CorpusID:88512404>

D6.7 Influence of aftershocks and clustered seismicity on seismic fragility



Šipčić, N., Kohrangi, M., Papadopoulos, A. N., Marzocchi, W., & Bazzurro, P. (2022). The Effect of Seismic Sequences in Probabilistic Seismic Hazard Analysis. *Bulletin of the Seismological Society of America*, *Xx*, 1–16. <https://doi.org/10.1785/0120210208>

Spillatura, A., Kohrangi, M., Bazzurro, P., and Vamvatsikos, D., 2021. Conditional spectrum record selection faithful to causative earthquake parameter distributions. *Earthquake Engineering and Structural Dynamics*, *50*(10), 2653–2671. DOI: 10.1002/eqe.3465

Vamvatsikos, D., and Cornell, C. A., 2002. The Incremental Dynamic Analysis and Its Application To Performance-Based Earthquake Engineering. *European Conference on Earthquake Engineering*, 10.

Weatherill, G., Kotha, S. R., and Cotton, F., 2020. A regionally adaptable “scaled backbone” ground motion logic tree for shallow seismicity in Europe: application to the 2020 European seismic hazard model. *Bulletin of Earthquake Engineering* (Vol. 18). Springer Netherlands. DOI: 10.1007/s10518-020-00899-9

Zhuang, L., Yin, P., and Pang, Y., 2022. E-Cloud: Efficient seismic fragility assessment of structures based on enhanced cloud analysis. *Earthquake Spectra*, 875529302211032. DOI: 10.1177/87552930221103290